Science and Technology Indonesia
e-ISSN:2580-4391 *p*-ISSN:2580-4405
Vol. 9, No. 2, April 2024

Research Paper

Preparation of PAN/PVDF Nanofiber Mats Loaded with Coconut Shell Activated Carbon and Silicon dioxide for Lithium-Ion Battery Anodes

Muhammad Rama Almafie[1,2,3,5], Rahma Dani[3], Riyanto[4], Leni Marlina[3], Jaidan Jauhari[5], Ida Sriyanti[3,5]*

[1]*Doctoral of Mathematics and Natural Sciences, Faculty of Mathematics and Natural Sciences, Universitas Sriwijaya, Palembang, 30139, Indonesia*
[2]*Doctoral of Engineering Science, Faculty of Engineering, Universitas Sriwijaya, Palembang, 30139,Indonesia*
[3]*Department of Physics Education, Faculty of Teacher Training and Education, Universitas Sriwijaya, Indralaya, 30662, Indonesia*
[4]*Department of Biology Education, Faculty of Teacher Training and Education, Universitas Sriwijaya, Indralaya, 30662, Indonesia*
[5]*Electronic and Nanotechnology Applications Research Group, Faculty of Computer Science, Universitas Sriwijaya, Palembang, 30139, Indonesia*
***Corresponding author**: ida_sriyanti@unsri.ac.id

Abstract
Utilizing carbon materials derived from natural biomass holds significant promise for battery applications, owing to their low cost, abundant availability, and environmentally sustainable characteristics. However, graphite anode materials do not meet the demands of efficient batteries. Coconut shell waste has the potential to be used as activated carbon in energy storage anodes. By adding silicon dioxide (SiO_2) to maintain structural stability and electrochemical reaction kinetics, the advantages of CCS can be maximized. Polyacrylonitrile/polyvinylidene fluoride (PAN/PVDF) composite polymer was used as a matrix to embed CCS/SiO_2 and synthesize nanofibers via electrospinning. The resulting nanofibers had diameters ranging from to 575–707 nm, with cross-linked, porous, and beadless characteristics. Mechanical properties were measured by single-fiber micro tensile tests. The young modulus, tensile strength, and toughness of each nanofiber were successfully maintained at 13.7 ± 0.4 MPa, 34.4 ± 0.1 MPa, and 982 ± 10 kJ/m^3, respectively, because of the presence of a β-crystal growth layer that facilitated efficient stress transmission. The reduction-oxidation process response had a potential difference of less than 1.286 V in the first cycle, whereas for the third and fifth cycles, it was maintained below 3.416 V. The lithium-ion diffusion coefficient was below 4.73×10^{13} cm^2/s. Using the anode directly, as in lithium-ion batteries, provided a high capacity of 382 mAh/g after 200 cycles. Good cycle stability, with over 98% retention of the initial capacitance after 200 charge/discharge cycles, underscores its potential for application in lithium-ion batteries.

Keywords
Capacity, Cycle, Impedance, Capability, Diffusion

Received: 18 December 2023, Accepted: 17 March 2024
https://doi.org/10.26554/sti.2024.9.2.427-447

1. INTRODUCTION

Lithium-ion batteries (LIB) currently hold a dominant position in the battery market due to their inherent characteristics such as a high specific capacity and voltage, high energy density, excellent cycle performance, low self-discharge rate, absence of memory effects, wide operating temperature range, and long service life. These attributes highlight the superiority of LIBs as power sources compared to other batteries (Nzereogu et al., 2022). Extensive research on electrode components, such as anodes and cathodes, has resulted in improved performance and reduced manufacturing costs. Graphite is often utilized as an anode material in commercial lithium-ion batteries; however, its limited rate capability and low theoretical specific capacity make it inadequate to meet the increasing demand for highly efficient batteries (Gao et al., 2022). Researchers have conducted extensive studies on carbonaceous materials, such as carbon nanotubes, graphene, and activated carbon, to improve the performance of lithium-ion batteries (LIBs). Activated carbon (AC) is a promising material due to its high porosity, low cost, environmental friendliness, extensive surface area, and exceptional electrical conductivity (Kalu Uka et al., 2022). Porous carbon has generated considerable interest due to its several appealing qualities, including high porosity, exceptional electrical conductivity, adjustable porosity, and remarkable stability under various chemical, thermal, and mechanical conditions. The hydrophobic nature of its surface coupled with its low density, chemical inertness, and ease of handling further enhances to its attractiveness. Moreover, its low cost makes it highly accessible (Wang et al., 2022d). Carbon-based materials derived from natural biomass have gained popularity due to their low cost, abundant availability, and environmentally friendly

nature. Hence, the production of low-cost activated carbon from biomass waste, such as coffee peels (Figueroa Campos et al., 2021), corn cobs (Medhat et al., 2021), rice straw (Khoshnood Motlagh et al., 2022), wheat straw (Zhang et al., 2022a), and coconut shells (Keppetipola et al., 2021), has garnered significant attention. When coconut waste is not optimally utilized, its production leads to the creation of shell waste (Darmawan et al., 2022) and fibers (Wang et al., 2022b), which can be utilized in various industries such as coconut oil (Suryani et al., 2020), coconut fiber (Sirisangsawang and Phetyim, 2023), and coconut desiccation (Marques et al., 2019). The typical makeup of coconut shells, which are an agricultural industrial waste and a natural source of fiber, typically consists of cellulose, hemicellulose, and lignin (Anuchi et al., 2022; Fatmawati et al., 2023). The global coconut cultivation area is estimated to be approximately 12 million hectares. The coastal and subtropical islands of the Philippines, India, Indonesia, Sri Lanka, Malaysia, Thailand, and Oceania make up a substantial portion of the total area planted with these crops, accounting for about 86% of the total planted area (Descals et al., 2020; Rethinam and Krishnakumar, 2022). Therefore, proposing the utilization of shell waste as a raw material for producing high-economic-value products like activated carbon and graphene has been suggested.

Silicon dioxide (SiO_2) has emerged as a promising alternative to traditional commercial graphite anodes for use in next-generation high-performance lithium-ion batteries (LIBs). This is due to its impressive high theoretical capacity and operating potential. Despite its encouraging attributes, the use of SiO_2 is hindered by significant volume fluctuations (300%) and inadequate conductivity, resulting in diminished capacity and inferior rate capability (Si et al., 2022). Researchers have sought effective solutions for this issue. One such solution involves combining silicon dioxide with carbon entropy to enhance structural stability and electrochemical reaction kinetics. SiO_2/C composites have two advantages over pure silicon dioxide for lithium storage. First, the flexible entropic carbon component of the composite resists mechanical strain and acts as a protective shield, stabilizing both electrode and electrolyte interfaces (Renman et al., 2021). The SiO_2/C composite's high conductivity, particularly that of its carbon component, contributes to an overall increase in conductivity. This results in enhanced cycle life and rate capability. For illustration, the discharge/charge capacitances of the SiO_2/C and SiO_2/C/graphene composites after 100 cycles were 428.5/426.5 and 610/605 mAh/g, respectively. The Porous SiO_2/C and SiO_2/C/graphene electrodes exhibit superior electrochemical performance compared to SiO_2/C electrodes, demonstrating a remarkable capacity retention of 97% over 100 cycles (Xiang et al., 2017). The Si/SiO_2/C composite displayed exceptional performance, achieving an initial discharge capacitance of 2860.3 mAh/g and an impressive initial cyclic retention of 86.7%. Even after 150 cycles, the composite demonstrated remarkable durability, retaining a capacity of 1389.8 mAh/g (Chen et al., 2021). The SiO_2/C composite, functioning as a freestanding anode material, demonstrated remarkable initial discharge and charge capacities of 1800 and 984 mAh, respectively. Additionally, it maintained a charge capacity of 754 mAh even after 200 cycles while maintaining a coulombic efficiency of 100% (Belgibayeva and Taniguchi, 2019). The development of SiO_2-C composites for enhancing capacitance during cycling, improving performance efficiency, and ensuring stable electrochemical retention has garnered considerable attention.

To optimize the benefits of SiO_2/C in Li storage, researchers have devoted efforts toward developing and fabricating hollow micro/nanostructures characterized by substantial surface areas, extensive interior cavities, and thin walls (Liu et al., 2021b). This hollow structure addresses volume variation by increasing the number of active sites for electrochemical reactions, reducing the distance for electron and lithium-ion diffusion, and enhancing the electrochemical kinetics, ultimately leading to improved structural stability (Wang et al., 2021). Production of nanofibers through electrospinning is an effective technique for generating hollow, porous, and large-surface structures using polymers as matrices. The application of nanofibers as components for anodes, cathodes, and separators has garnered significant interest in recent years (Cao et al., 2023). The fabrication of nanofibers requires at least one conductive polymer as the matrix, such as polyacrylonitrile (PAN) (Lee et al., 2022), polyvinylidene fluoride (PVDF) (Gong et al., 2019), polyethersulfone (PES) (Liu et al., 2021a), and polypropylene (PP) (Hu and Lin, 2021; Moghim et al., 2022). Active materials can be derived from semiconductor materials, such as SiO_2 and TiO_2, and carbon-based materials, such as graphene (Liu et al., 2021b), carbon nanotubes (Gonzalez et al., 2022), and graphite (Rey et al., 2021). PAN offers high flexibility, easy integration, and high conductivity. The qualities of PAN and PVDF allow them to form extensive networks of imine chains through the polymerization of nitrile groups, with the inner C≡N groups bonding with lithium ions. Moreover, PAN can be easily copolymerized because of its chemical reactivity. PVDF, despite displaying semi-crystalline properties, demonstrates remarkable mechanical strength, outstanding thermal stability, high chemical resistance, and exceptional hydrophobicity. These attributes render PVDF an optimal material for safeguarding electrodes from harm and extending battery cycle duration (Aghayari, 2022). The exceptional hydrophobic properties of PVDF contribute significantly to its superior compatibility with Li.

In this research, we expanded upon prior findings by revealing the structure of PAN/PVDF/SiO_2 composite nanofiber-infused coconut shell activated carbon and incorporated silicon dioxide, which was then engineered and prepared as a top-performing anode material for lithium-ion batteries (LIBs). The activated carbon acted as a conductive scaffold to guarantee exceptional electrical conductivity and swift electron transport during the charging and discharging processes. Employing carbon derived from affordable and eco-friendly natural biomass, such as coconut shells, presents a promising solution due to its low cost, abundance, and environmental sustainability. How-

ever, silicon dioxide (SiO_2) is plagued by significant variations in volume and poor conductivity, which results in decreased capacity and subpar rate capability as a high-performance anode option. Consequently, SiO_2/C composites were developed to enhance the stability of the electrode and electrolyte interfaces, thereby increasing the conductivity of the entire composite. The incorporation of conductive polymers, such as polyacrylonitrile (PAN) and polyvinylidene fluoride (PVDF), facilitates interactions between the functional groups of the polymer and lithium ions. Recently, it has been demonstrated that the combination of conductive polymers and carbon-based materials in nanofiber composites increases nanofiber permeability while decreasing electrical loss and flexibility. Coconut-shell-activated-carbon-embedded PAN/PVDF/SiO_2 composite nanofibers are emerging materials that hold great potential for use as anodes in lithium-ion batteries (LIBs) due to their distinctive characteristics.

2. EXPERIMENTAL SECTION

2.1 Materials

This study used the coconut-shell waste obtained from a local market in South Sumatra Province, Indonesia, which underwent four stages of processing: purification, carbonization, catalysis, and drying. Iron (III) chloride ($FeCl_3$, CAS 10025-77), zinc chloride ($ZnCl_2$, CAS 98 7646-85-7), and hydrochloric acid (HCl, CAS 37 7647-01-0) were obtained from PT. Brataco Chemika (Indonesia). Lithium iron (II) phosphate ($LiFePO_4$, CAS 15365-14-7) polyethylene (PE) (CAS 9002-88-4), PAN (Mw 150,000 kg/mol, CAS 25014-41-9), and PVDF (Mw 534,000 kg/mol, CAS 24937-79-9) were purchased from Sigma-Aldrich (Singapore). N, N-dimethylformamide (DMF, ≥ 99.8% Assay, CAS 68-12-2) was procured from VWR Chemicals BDH (Singapore). Silicon oxide (SiO_2 CAS 14808-60-7) was obtained from PT. Brataco Chemika (Indonesia). LiCl (CAS 7447-41-8) was purchased from Merck (Singapore).

2.2 Preparation of Coconut Shell Activated Carbon

The preparation method for coconut shell activated carbon (CCS) was adapted from Jauhari et al. (2021) and Almafie et al. (2022). The CCS waste was dried under the sun for about six days and ground into a powder using a bulk mill with a 180-200 mesh. Carbonization and activation were achieved in two stages using $FeCl_3$, $ZnCl_2$, and urea as pyrolysis catalysts, activating agents, and nitrogen sources, respectively. A mixture of raw CCS powder, $ZnCl_2$, and urea in 1 M $FeCl_3$ was stirred at 80 °C on a hot plate for 2 hours. The resulting solid material was then separated by freeze-drying in an oven for 1 hour. The dried material was then placed in a tube furnace and charged with nitrogen. The material was heated in a furnace to 250 °C over a period of 45 minutes, and then maintained at that temperature for an additional hour. Afterward, the temperature was raised to 900 °C, and the material was graphitized for 90 minutes under a nitrogen flow. The resulting graphite had traces of Fe impurities, which were eliminated by soaking the crude product in 2 M HCl solution for 2 hours, followed by rinsing with distilled water and drying at 105 °C to a constant mass.

2.3 Preparation of PAN/PVDF/SiO_2-CCS Nanofiber Composite

A PAN/PVDF polymer solution, which can serve as a matrix, was prepared by dissolving 12 wt% PAN and 6 wt% PVDF in 82 wt% DMF. The mixture was subsequently heated to a temperature of 80 °C and continuously stirred for four hours. Following this, silicon dioxide was added, and the mixture was stirred for another three hours. After that, carbon coated silica was added until a homogeneous solution with good viscosity was achieved after four hours. This resulted in the formation of the SiO_2-CCS embedded PAN/PVDF (PAN/PVDF/SiO_2-CCS) precursor solution. The process was repeated while varying the concentrations of SiO_2 and CCS across six different levels, as shown in Table 1. The precursor solution was dispensed using a 5 mL disposable syringe (Terumo, Singapore) with a 24-gauge needle, connected to an electrospinning device (Nanolab ES106, Malaysia). The device consisted of a pump, a direct current power supply attached to the nozzle, and an aluminum-coated metal collector. The formation of composite nanofibers from precursor solutions is a result of the process known as electrospinning. The schematic for the PAN/PVDF/SiO_2-CCS experiment is illustrated in Figure 1 During the experiment, a positive voltage of 15 kV was applied, and the extrusion speed was set at 0.25 mm/min. The distance between the collector tip and needle was set at 20 cm. The experimental conditions were maintained at a temperature of 25 °C and a humidity level of 40–50% within a controlled environment.

Table 1. Composition of the PAN/PVDF/SiO_2-CCS Precursor Solution

Sample	PAN (wt%)	PVDF (wt%)	CCS (wt%)	SiO_2 (wt%)
SBE1	12	6	10	5
SBE2	12	6	10	7
SBE3	12	6	10	9
CBE1	12	6	12	11
CBE2	12	6	14	11
CBE3	12	6	16	11

2.4 Electrochemical Performance Tests

The nanofibers used as anodes were assembled into cells for electrochemical performance tests, performed by arranging separators, cathodes, and anodes. The anode, cathode, and separator for the nanofiber composite were PAN/PVDF/C-SiO_2, $LiFePO_4$, and PE, respectively. The average mass loading of the nanofiber was approximately 9 mg, with each electrode measuring 100 μm in thickness. Before the combination of

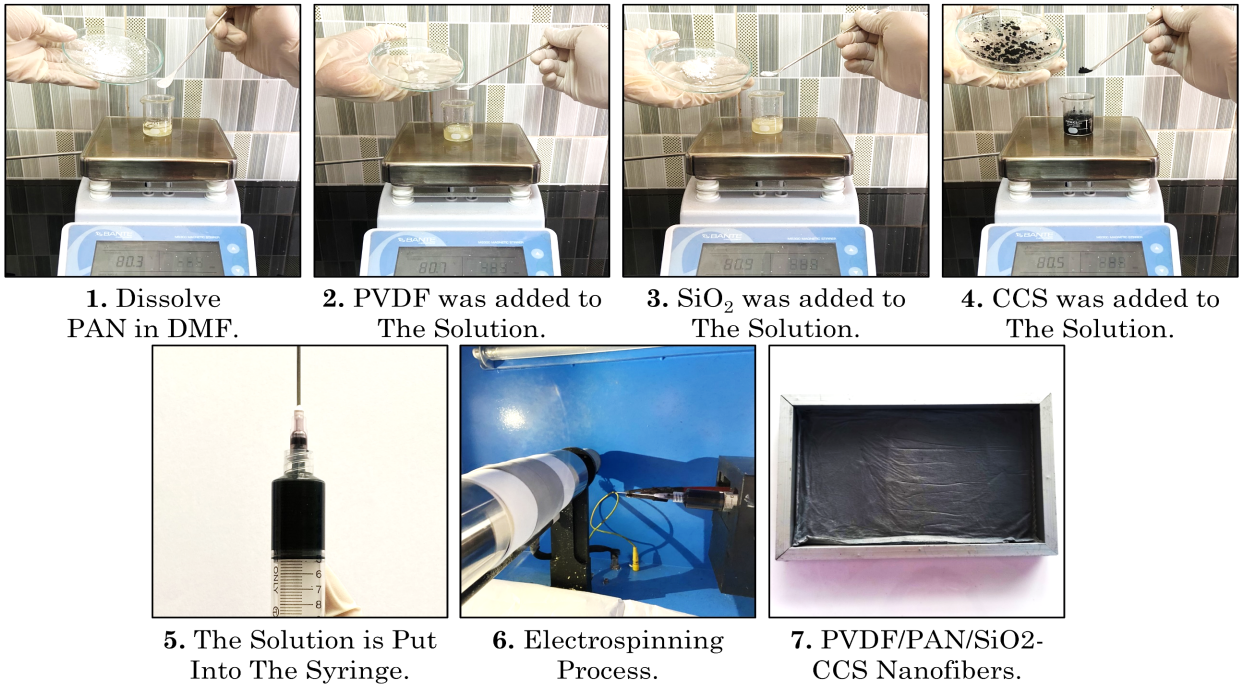

Figure 1. Schematic of the PAN/PVDF/SiO_2-CCS Experiment. Photograph: Courtesy of Rahma Dani. Copyright 2023.

the cathode and anode, a separator was inserted as a barrier to prevent their interaction. The anode and cathode were placed on separate copper foils, with the cathode additionally mounted on an aluminum foil serving as a current collector. It was wrapped in plastic wrap with a hole in the top center to facilitate the entry of the electrolyte. Subsequently, it was closed again using thicker plastic to prevent electrolyte leakage. The cathode and anode were assembled in an empty sleeve and compressed continuously. The electrolyte-free battery was administered with a 20% LiCl solution as its electrolyte. All of the lithium cells were assembled in a glove box, and the humidity inside the box was kept below 0.5%.

2.5 Structural Characterization

Scanning electron microscopy analysis was conducted using a Vega3 instrument (Tescan (USA), Japan) and JEOL JSM 6510 LA instrument (Japan). Electron micrographs were obtained at an accelerating voltage of 25.0 kilovolts. A small segment of each sample was coated with gold before being examined. The ImageJ software from the National Institutes of Health was utilized to evaluate the electronic micrographs and determine the average diameter at roughly 100 different locations. Samples were tested at a temperature of 25 °C and relative humidity of 65% using a universal testing machine (ZwickRoell, Germany) with a load cell capacity of 50 N and a cross-head speed of 10 mm/min. Four samples, each measuring 0.05 mm × 10 mm in cross section, were tested for each type of scaffold, with a gauge length of 20 mm (ASTM D882-02). Intermolecular bonding and functional group properties were assessed using Fourier transform infrared (FTIR) spectroscopy (8201PC Shimadzu, Japan) in the attenuated total reflectance (ATR) mode. The specific surface areas and pore size distributions were studied using a Brunauer–Emmett–Teller (BET) nitrogen absorption isotherm physisorption instrument (Quadrasorb-SI-4-Kr, MP Quantachrome, USA). Cyclic voltammetry (CV) (Corrtest Electrochemical Workstation CS350) is an electroanalytical method, which is based on the principle of electrolysis of a solution containing electroactive analytes; the reaction occurs at the metal electrode with the electrolyte solution. CV measurements were performed between 1.5 and 3.0 volts at various scan rates in order to obtain accurate results. Galvanic charge–discharge (GCD) characteristics are used to determine the ability of a material to store energy. Charge/discharge testing was carried out using the Corrtest Electrochemical Workstation CS350 tool in the GCD mode on a test system battery at various current densities within a potential window of 1.6-2.8 V. The energy capacity or charge was expressed as mAh/g. Charge-discharge tests were conducted at a constant current density. Electrochemical impedance spectroscopy (EIS) (Corrtest Electrochemical Workstation CS350) was used to analyze the electrode for AC potential signals at low amplitudes (~ 10 mV) over a wide frequency range. The voltage of 0.10 V with a frequency range of 0.01-10^5 Hz was used.

2.6 Statistical Analysis

The pharmacokinetic parameters were analyzed statistically using OriginPro 2021 for Windows, Version 9.8 (OriginLab Corporation, USA), with one-way ANOVA and Tukey's hon-

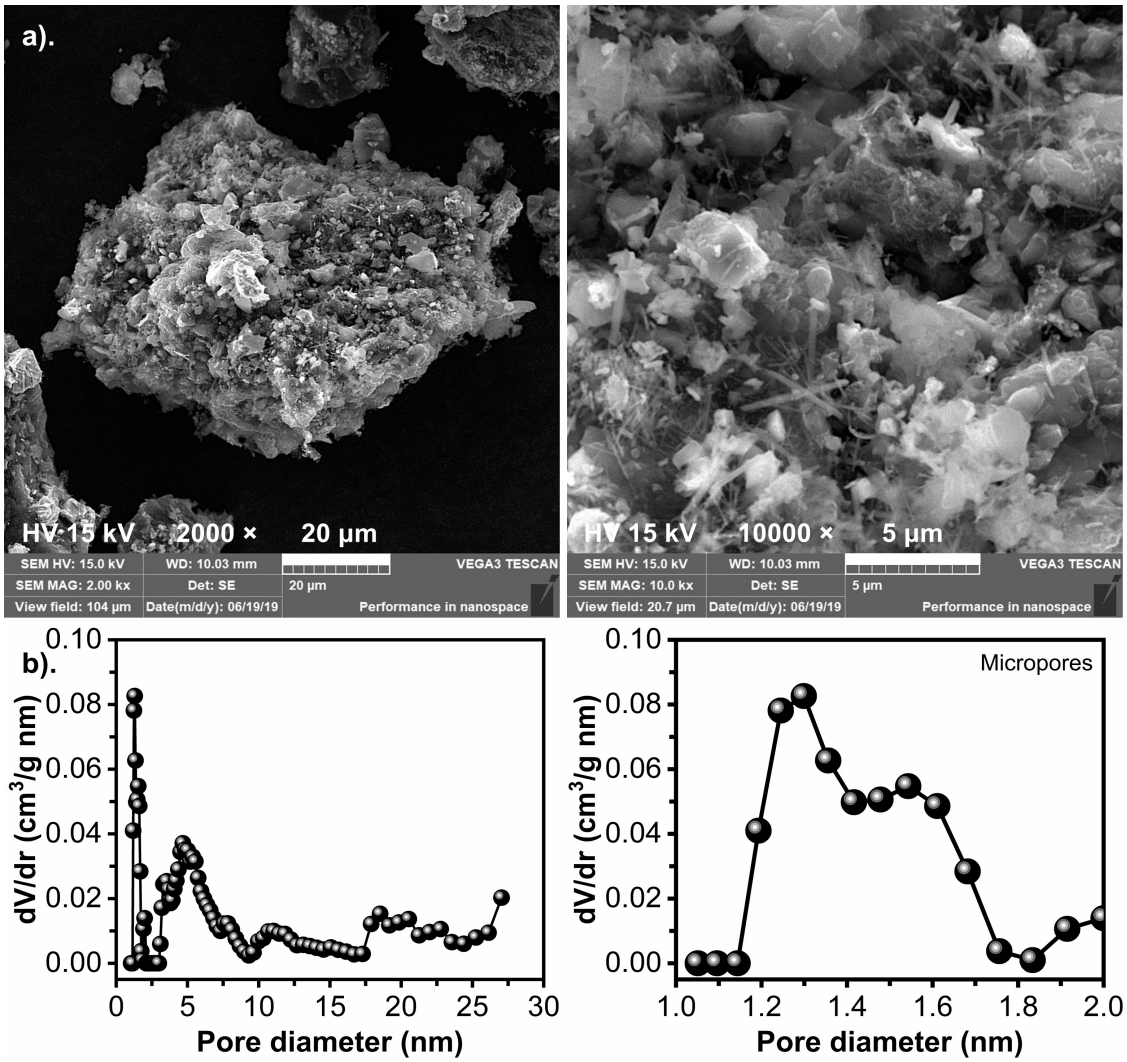

Figure 2. SEM Images of CCS: (a) Magnification: 2000× and 10.000× (b) BET Pore Size Distribution

estly significant difference (HSD) as post-hoc tests (Almafie et al., 2022). Differences between results were considered significant at the $p < 0.001$ and $p < 0.05$ levels.

3. RESULTS AND DISCUSSION

3.1 Coconut Shell Activated Carbon (CCS)

Employing scanning electron microscopy (SEM) enabled the examination of the activated carbon's surface morphology derived from coconut shells. The results demonstrate a heterogeneous arrangement of nanosheet structures and rough surfaces, as depicted in (Figure 2a). Pyrolysis was employed to manufacture the CCS. Pyrolysis entails the thermal decomposition of a lignocellulosic biomass matrix without the presence of oxygen at elevated temperatures (Shafizadeh et al., 2023). The ability of a biomass to produce various solid, liquid, and gaseous products makes it a versatile resource. Decomposition of cellulose, hemicellulose, and lignin at 500 °C during carbonization yields a range of valuable products (Bag et al., 2020). Physical activation at elevated temperatures does not result in larger pore formation but rather leads to the formation of broken nanosheets. This nanoscale structure provides a more active location for electric double layer formation, increases open surface area, facilitates diffusion of electrolyte ions, and prevents nanosheet accumulation. When the carbonization temperature reached 600 °C, the surface morphology changed, and the activated carbon appeared in larger forms with expanded pores. The formation of mesopores on the surface is a direct consequence of high-temperature physical activation (Duan et al., 2021).

The BET test results show that there is still a micropore structure (Figure 2b). The extensive porosity of the nanosheets adorned with fibers provides a significant concentration of micro- and mesoporous active sites for ions to establish an electrical double layer in addition to channels that facilitate diffusion and expedite the rate of ion transformation. The diminution or elimination of the fiber surface occurs when the

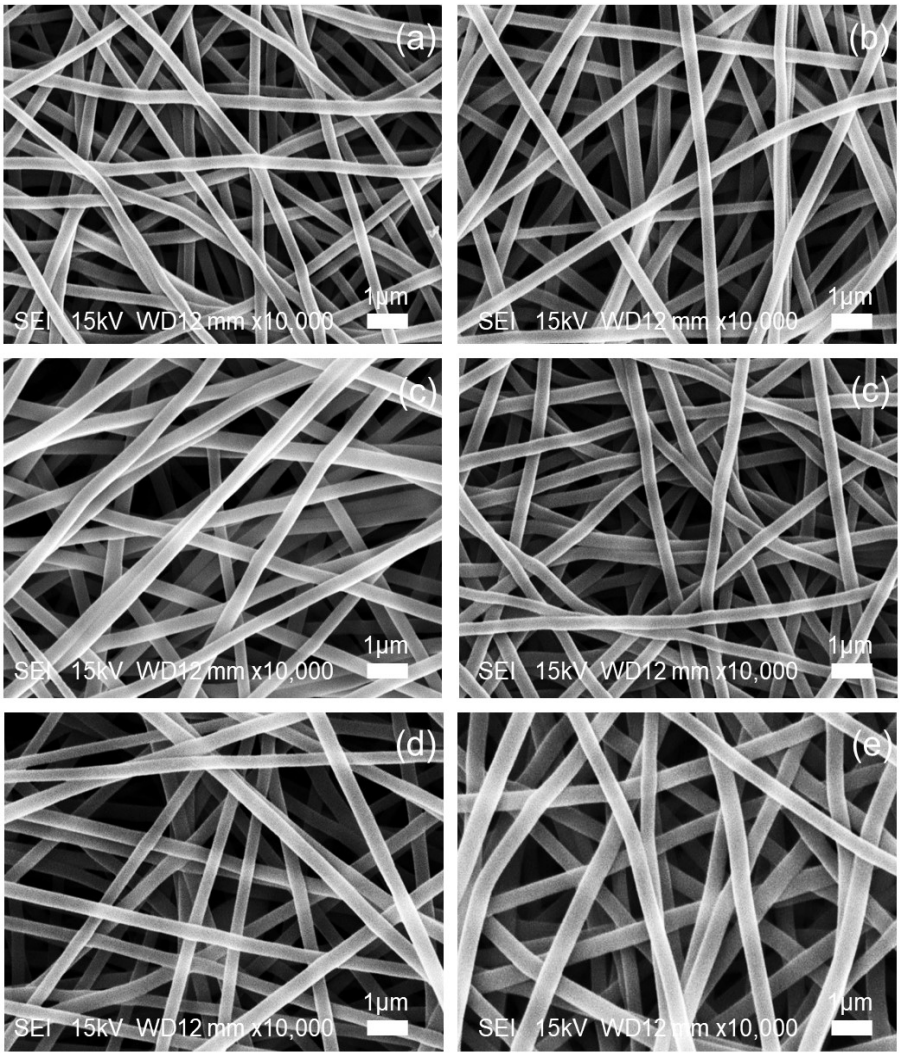

Figure 3. SEM Images of the PAN/PVDF/SiO_2-CSS Nanofiber Composites: (a) SBE1, (b) SBE2, (c) SBE3, (c) CBE1, (d) CBE2, and (e) CBE3

carbonization temperature exceeds 700 °C, at which cellulose and hemicellulose degrade completely, thereby giving rise to small flower-like nanosheets (Bag et al., 2020). Furthermore, in addition to micro- and mesopores, an extensive network of macropores that has been intentionally engineered to expedite ion transport is present. The production of nanosheets with lower lignin contents results in the creation of much smaller structures, whereas larger nanosheets can be reduced in size through fragmentation. The remarkable achievement of the activated carbon material, derived entirely from coconut shells without any synthetic additives, lies in its exceptional performance in the field of high-performance energy-storage devices. This accomplishment is a standout in the realm of energy storage and demonstrates the potential for sustainable and eco-friendly solutions in this field.

3.2 PAN/PVDF/SiO_2-CCS Nanofiber

Electrospinning is a process that employs static electricity to produce nanofibers and microfibers. This method entails applying a high voltage to an injected polymer solution, which leads to the formation of electric jets that create the desired outcome. Electrospinning setup generally includes a grounded collector, high-voltage power source, syringe pump, and metal needle (Cao et al., 2023). The process of creating PAN/PVDF/SiO_2-CCS nanofiber composites depends heavily on the interaction between the charged polymer precursor and an external electric field. A high voltage is necessary to achieve the desired results. As the voltage increased, the dispersed phase of the solution flowed as droplets, resulting in spraying and formation of nanoparticles. The physical, chemical, and mechanical characteristics of the resulting polymer nanofibers depend on various factors, including the solution parameters, electrospinning voltage, speed, and distance between the needle and receptor

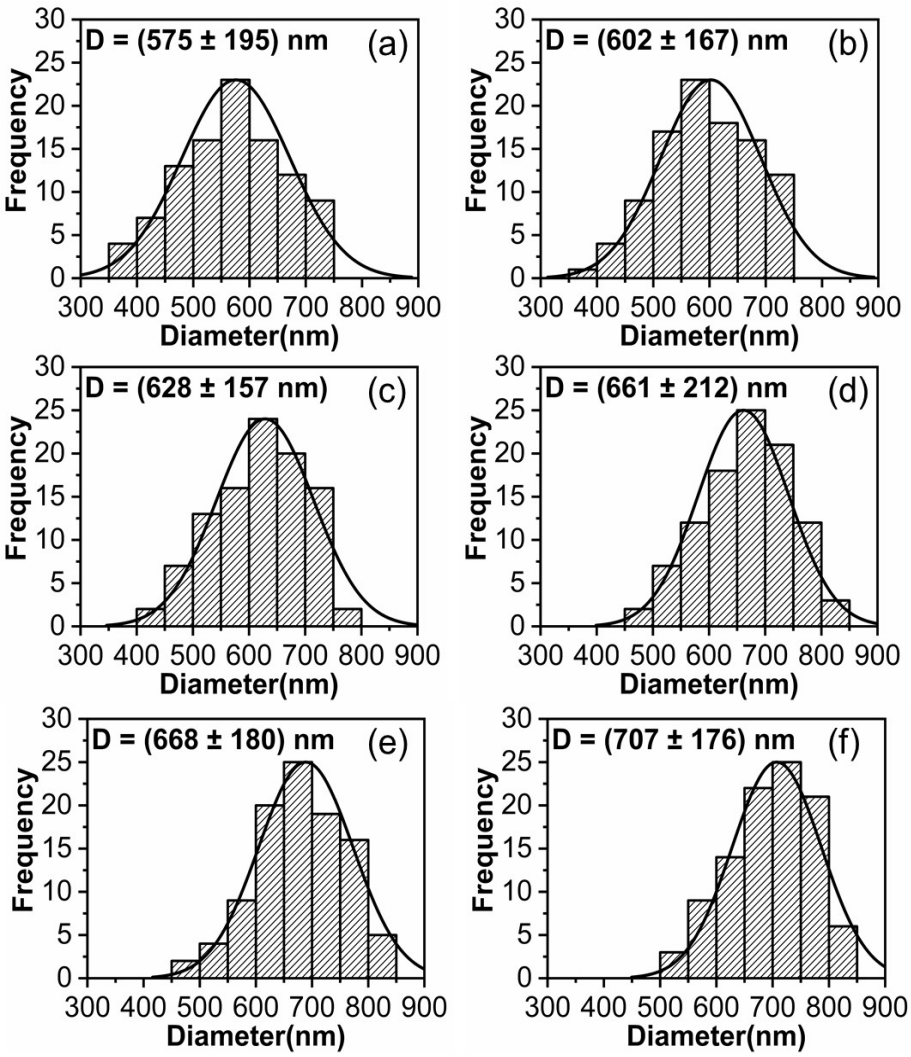

Figure 4. Distribution Diameter of the PAN/PVDF/SiO_2-CSS Nanofiber Composites: (a) SBE1, (b) SBE2, (c) SBE3, (c) CBE1, (d) CBE2, and (e) CBE3

surface (Wang et al., 2022b). SEM confirmed the microstructure of the composite nanofibers. The six samples displayed a clear nanofiber structure under SEM at a magnification of 50,000×, revealing a smooth and uniform surface. As shown in Figure 3, the addition of SiO_2 and CCS did not affect the formation characteristics of the nanofibers; however, the diameter distribution increased with the addition of these substances. These results are in accordance with those of Sriyanti et al. (2021), who found that increasing the extract concentration reduces the nanofiber diameter. Jauhari et al. (2021) did not observe any changes in nanofiber morphology, and this was attributed to the fluctuations in the viscosity of the polymer solution as the solution concentration increased.

The average diameters of the nanofibers obtained from the SBE1 and CBE1 solutions were 575 ± 195 and 661 ± 212 nm, respectively, exhibiting a more uniform distribution. However, the average diameters of the SBE3 and CBE3 nanofibers were 628 ± 63 nm and 707 ± 68 nm, respectively, as shown in Figure 4. These diameters are lower than that of the graphene oxide/polyacrylonitrile composite fibers (1506 ± 61 nm) applied to supercapacitor electrode membranes (Jauhari et al., 2021). The diameter of the core-shell structured PAN/PVDF nanofiber utilized as a stable lithium-based battery separator was measured at 625.65 nm (Gao et al., 2023). Statistical analysis was performed using one-way ANOVA and Tukey's HSD test to determine the statistical significance of the differences between samples, as shown in Figure 5. The findings indicated that there were no substantial discrepancies between the nanofiber composites at a significance level of $p < 0.05$. The coefficient of variation, calculated as the ratio of the standard deviation to the mean diameter, was employed to evaluate the uniformity of the distribution. The SBE1 and CBE1 nanofibers exhibited a nonuniform distribution with a coefficient of variation greater than 0.3 (Almafie et al., 2022). Due

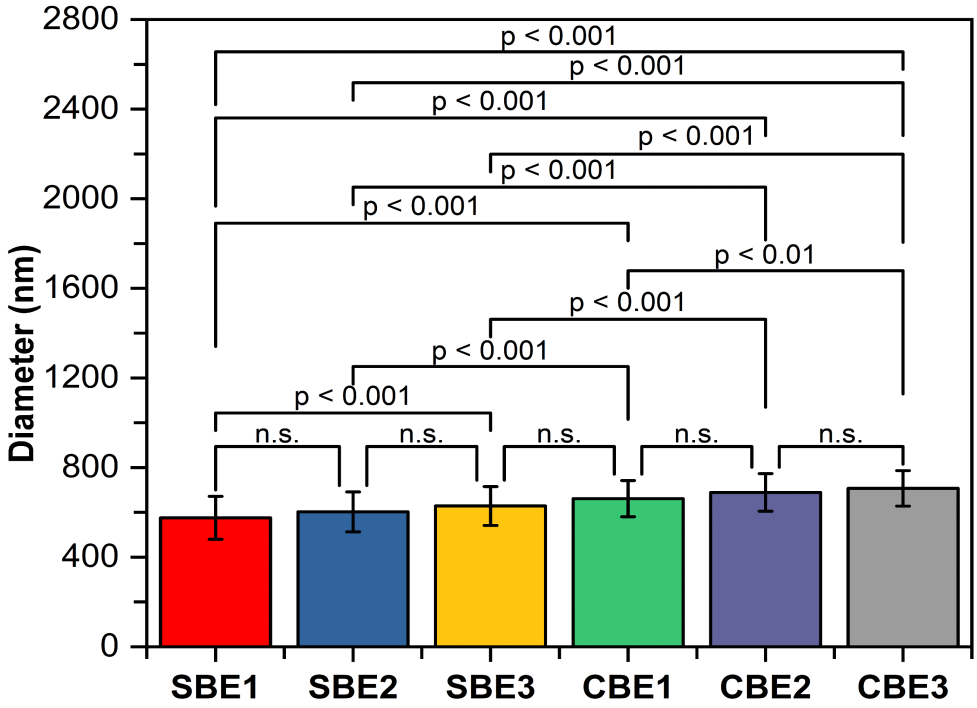

Figure 5. Paired Comparison of the Diameters of the PAN/PVDF/SiO_2-CCS Nanofiber Composites

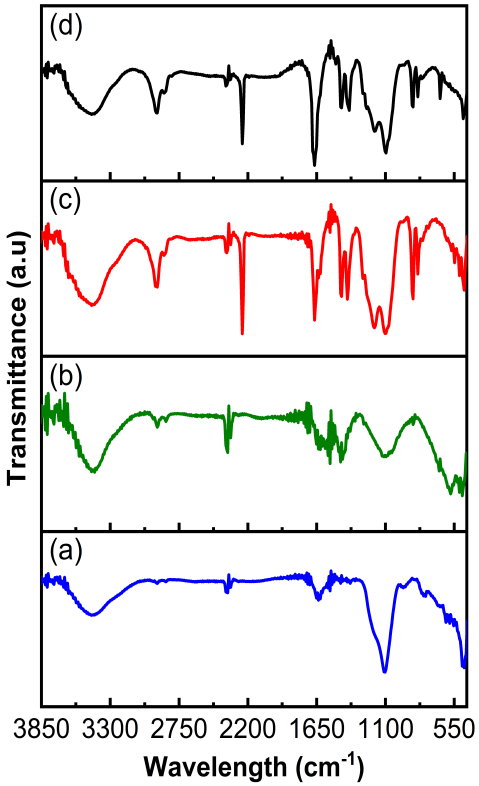

Figure 6. FTIR Spectra of (a) SiO_2, (b)CCS, (c) PAN/PVDF, and (d) PAN/PVDF/SiO_2-CCS Nanofiber Composites

to the robust electric field, the applied force on the fiber increased, resulting in a rise in fiber diameter. The solution's electric charge is essential for attaining the desired fiber diameter. An increase in the electric charge leads to a higher dielectric constant, resulting in more force being applied to the jet under an electric field, causing the formation of smaller fibers. The viscosity of the solution is another critical parameter in the electrospinning process. A decrease in viscosity leads to the production of thinner fibers (Wang et al., 2022b). The incorporation of SiO_2 and CCS during the fabrication process enhanced the electrical charge and viscosity, thereby increasing the fiber diameter. Consequently, the percentage in the solution increases, leading to alterations in the uniformity of the fiber morphology. Although the addition of SiO_2 and CCS had minimal impacts on the nanofiber structure, it significantly influenced the nanofiber diameter.

3.3 FTIR Analysis

FTIR spectroscopy was performed to confirm the interaction and cross-linking between the spectra at 550 and 3850 cm^{-1}. The spectrum of the SiO_2 powder (Figure 6a) showed a characteristic absorption peak at 3410 cm^{-1}, corresponding to the O−H stretching vibrations of incomplete Si−OH silanol groups (Wang et al., 2022a). The characteristic absorption peaks of SiO_2, observed at approximately 1103, 965, and 756 cm^{-1}, can be attributed to asymmetric and symmetric Si−O−Si strain vibrations and Si−OH bending vibrations, respectively (Awadh and Yaseen, 2019; Ellerbrock et al., 2022). This is typical of amorphous SiO_2. The spectrum of the CCS

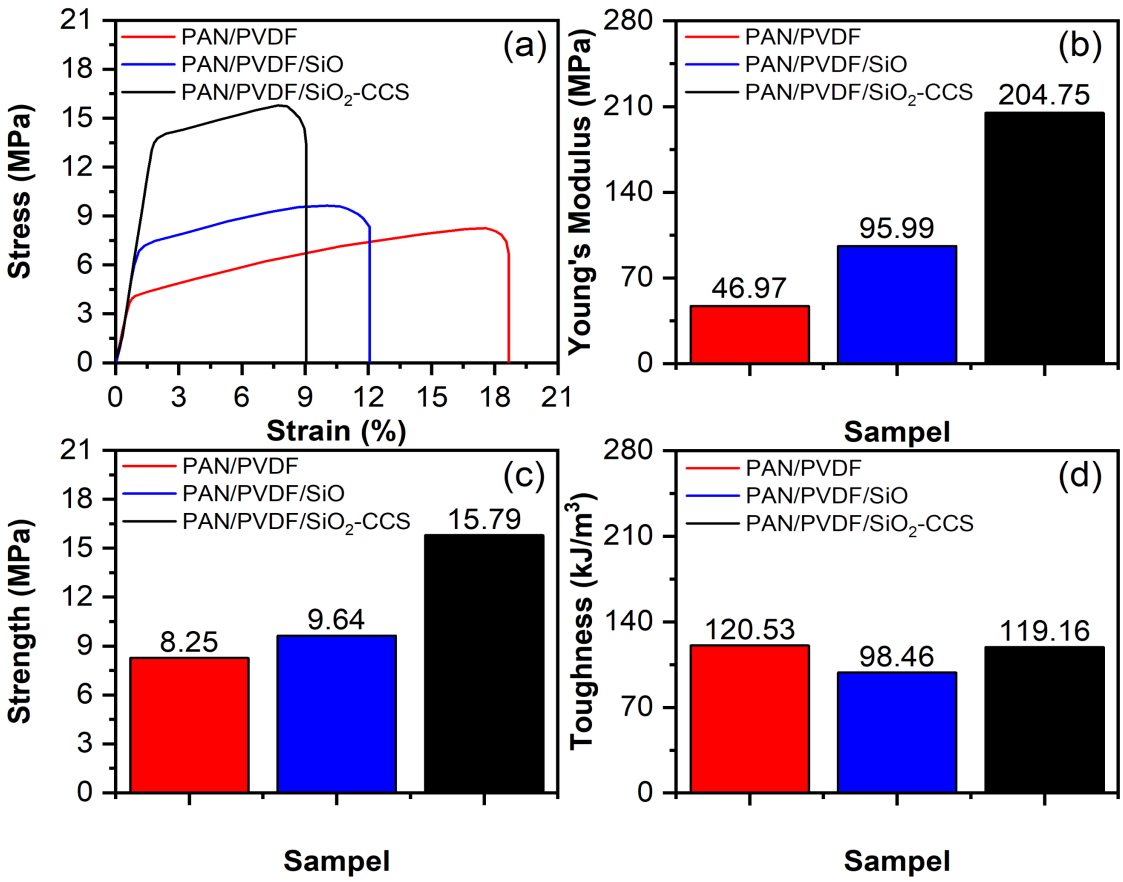

Figure 7. Mechanical Properties of Nanofiber Composite: (a) Stress-Strain Curve, (b) Ultimate Tensile Strength, (c) Young's Modulus, and (d) Toughness

powder (Figure 6b) showed a band corresponding to the stretching vibration of the hydroxyl group (–OH) at approximately 3425 cm^{-1} (Kanjana et al., 2021). The two bands at 2924 and 2854 cm^{-1} were assigned to the asymmetric and symmetric stretching vibrations, respectively, of the C−H group (Kanjana et al., 2021; Rodrigues et al., 2020). The relatively strong band at 1795 was attributed to the O−C=O group, formed by the esterification reaction between carboxyl and phenolic groups during the preparation stage (Rodrigues et al., 2020). The sharp bands at 1651 and 1637 cm^{-1} were assigned to the carboxylate stretch bands (Kanjana et al., 2021). The peak at 1543 cm^{-1} was caused by the C=O stretch (Nizam et al., 2021). However, the other peak at 1033 cm^{-1} was ascribed to the C−O−C stretching (Méndez et al., 2022).

The spectrum of PAN/PVDF (Figure 6c) exhibited peaks at 3448 and 2924 cm^{-1} corresponding to the strong interaction of N−H stretching and C−H stretching vibrations, respectively (Yasmeen et al., 2016). The peak located at 1452 cm^{-1}, associated with C−F stretching vibrations, was due to C−C bonding, and the weak peaks around 509 and 471 cm^{-1} were caused by CF_2 bending vibrations (El Sakhawy et al., 2018). In addition, the peak located at 1667 cm^{-1} was caused by the formation of a C=O double bond (Da Róz et al., 2010). The presence and interaction of PAN and PVDF in the composite matrix are indicated by the overlapping peaks in the C=O band region at approximately 1740 cm^{-1} and N=C−N amine group at 1643 cm^{-1} (Mohammed et al., 2021). The strong peak at 879 cm^{-1} was determined to be the dominant α phase, especially in the PAN/PVDF nanofiber, and the influence of the PVDF phase was observed in the bands around 879 and 784 cm^{-1}, representing the α and β phases, respectively (~1450, 1404, 1181, 1072, 841 cm^{-1}) (Sriyanti et al., 2023). The PAN/PVDF/SiO_2-CCS composite nanofiber exhibited features different from the changes in the infrared spectral peaks shown in Figure 6d. Strong interactions of N−H stretching and C=O stretching were observed in the ranges of 3700-3500 and 1790-1540 cm^{-1}, respectively, showing the typical pattern of PAN/PVDF (Sriyanti et al., 2023). The overlapping absorption bands located between 3200-2750 and 2430-2330 cm^{-1}, associated with the C−H stretching vibrations of alkane groups, experienced slight strengthening due to interference from CCS molecular interactions (Kanjana et al., 2021; Rodrigues et al., 2020). The presence of SiO_2 causes the α-crystalline phase to decrease, and this can be interpreted as the contribution of SiO_2 to fiber crystallization (Liu et al., 2021c). The β-phase characteristics of PVDF were 1095, 670, and 478 cm^{-1} were

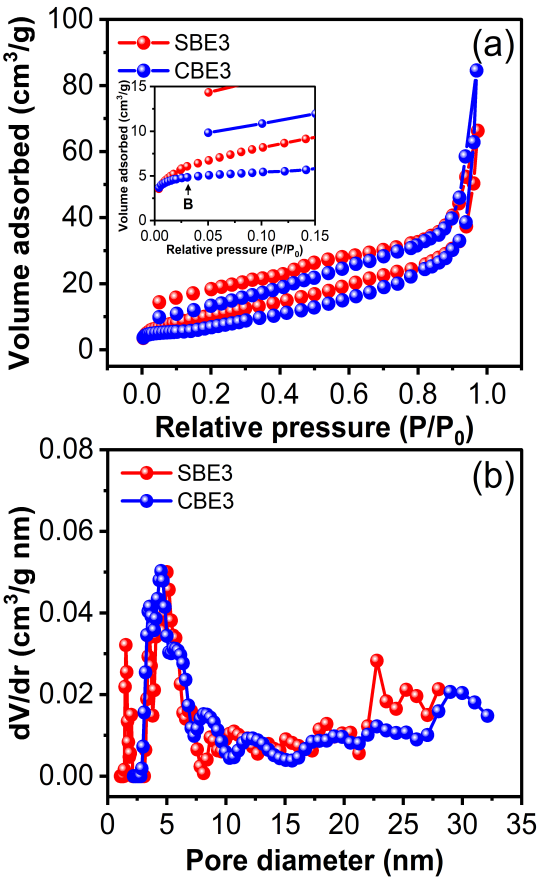

Figure 8. (a) Brunauer-Emmett-Teller (BET) Nitrogen Adsorption/Desorption Isotherms and (b) Pore Size Distribution Curves of SBE3 and CBE3

associated with the SiO_2 asymmetric strain, SiO_2 symmetric strain, and SiO_2 bending mode, respectively (Awadh and Yaseen, 2019; Ellerbrock et al., 2022).

3.4 Mechanical Properties

The mechanical performance of flexible electrodes is crucial for practical applications, particularly for carbonaceous anodes, which are prone to brittleness (Almafie et al., 2022). The mechanical properties of PAN/PVDF, PAN/PVDF/SiO_2, and PAN/PVDF/SiO_2-CCS nanofiber composites were influenced substantially by the increased amounts of SiO_2 and CCS, resulting in significant variations in their mechanical behavior. According to the data presented in Figure 7, the addition of these materials resulted in an increase in both Young's modulus and maximum tensile strength. The average Young's modulus and tensile strength of the PAN/PVDF composite, with the lowest values of 46.92 and 8.25 MPa, respectively, are greater than those of PAN/PVDF/SiO_2 (95.99 and 9.64 MPa, respectively). PAN/PVDF/SiO_2-CCS shows a relatively significant improvement compared to PAN/PVDF. Specifically, the Young's modulus and tensile strength are 204.75 and 15.79 MPa, respectively. Moreover, the PAN/PVDF composite exhibited the highest energy requirement for fracture (120.53 MJ/m^3). However, the toughness of the PAN/PVDF/SiO_2 composite (98.46 MJ/m^3) was slightly reduced compared to those of the other composites. In contrast, PAN/PVDF/SiO_2-CCS showed an exceptionally high toughness of 119.76 kJ/m^3. The enhanced mechanical characteristics of the composite can be attributed to the hydrogen bonding connections between the polymer matrix, SiO_2, and CCS (Nasser et al., 2020). The polymer matrix, coupled with the incorporation of SiO_2 and CCS, enhanced the bonding through interconnected networks, resulting in efficient stress transmission. This presents a significant advantage over conventional nanofiller inclusions, which typically lead to poor dispersion and a lower tensile strength and Young's modulus (Megahed et al., 2021). Furthermore, mechanical forces such as uniaxial tensile forces promote the growth of β-crystal layers, which comprise trans-gauche-trans-gauche (TGTG) and trans-trans (TT) conformational chains (Sriyanti et al., 2021; Su et al., 2021). The TGTG conformation exhibited a greater degree of stability than the TT conformation, resulting in the prevalence of α-crystals (Elele et al., 2019). PVDF nucleation involves the incorporation of SiO_2 and CCS, resulting in the formation of molecular chains with the TT conformation under a high-voltage electric field. The strain orientation process leads to the formation of β-phase crystallites, which enhance the mechanical properties of the fiber (Liu et al., 2021b). Therefore, it can be inferred that the components of the composite material affect its mechanical properties.

The mechanical characteristics of reinforced nanofibers play a crucial role in determining the tensile strength and Young's modulus of nanocomposites. The presence of anisotropy influences the structure and properties of nanofiber mats, ultimately affecting their strength The strength decreased when the nanofibers were randomly oriented but increased when they were oriented in a single direction (Aghayari, 2022). Nanofiber orientation also improved the tensile strength of the mats. The nanofiber mats collected at high speeds were mechanically better on flat-plate collectors. The mechanical properties of the nanofibers improved exponentially as their diameter decreased. The composition of the polymers, their molecular arrangement, and the length of their chains are factors that influence the tensile strength of the nanofiber mats (Khan et al., 2020). The way in which amorphous and crystalline phases are arranged, whether they are randomly or sequentially distributed, impacts the physical and mechanical properties of nanofibers. The orientation of polymer molecules during electrospinning is influenced by the electromagnetic force, which in turn determines the orientation of the polymer within the nanofibers (Belgibayeva and Taniguchi, 2019). The nanofiber mats' durability can be increased by employing a rotating drum collector with a higher rotational speed, which applies greater mechanical stress to the polymer molecules in a more concentrated manner (Rashid et al., 2021). The addition of nanofiber mats as laminates within polymer solution blends for epoxy-based composites resulted in a notable increase in the elastic modulus.

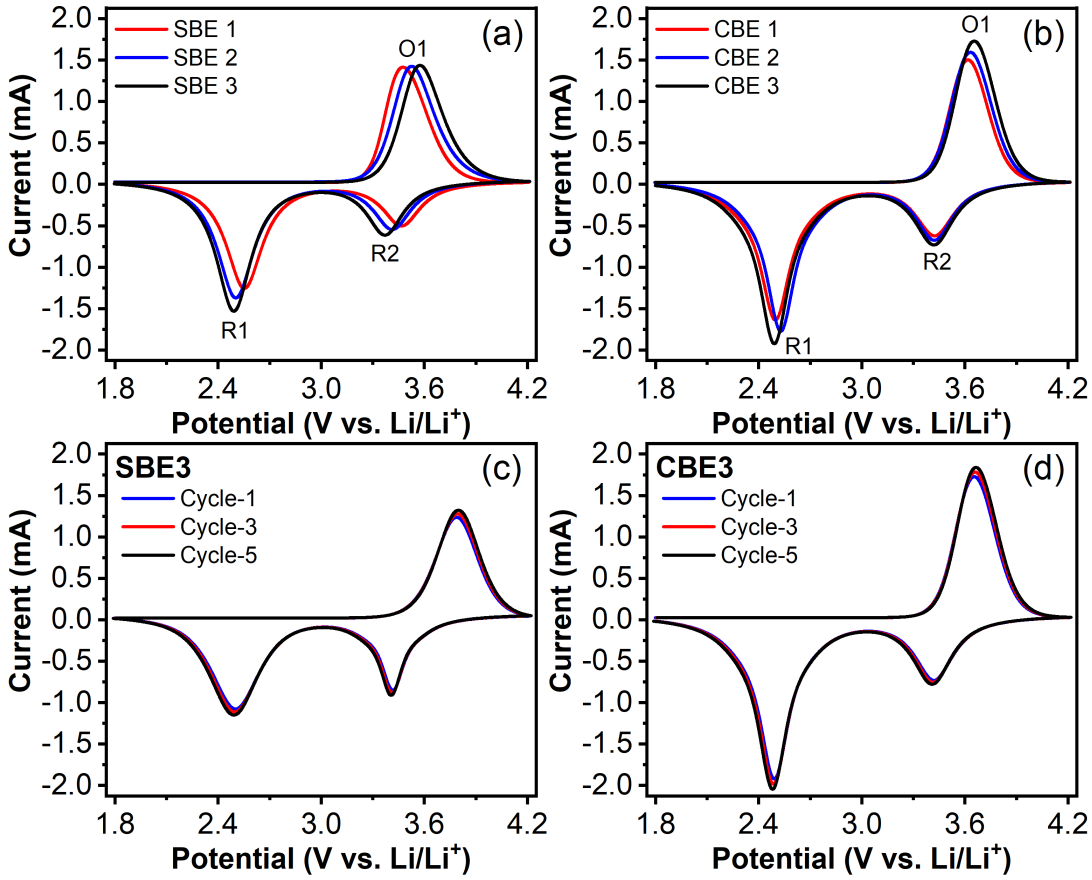

Figure 9. Cyclic Voltammogram Curves of Batteries with (a and b) SBE-CBE and (b and c) SBE3-CBE3, Up to the 5th Cycle, Recorded at a Constant Potential in the Range of 1.8–4.2 V with a Scan Rate of 1.0 mV/s

This increase was primarily attributable to the alignment of the nanofibers in the mats, which led to a reduction in fiber diameters and a favorable phase orientation of the polymer molecules.

3.5 Pore Structure Characteristics

Low-temperature nitrogen adsorption is a well-established and commonly utilized technique for measuring the specific surface area and pore-size distribution of materials. The amount of nitrogen that adsorbs onto a solid surface depends on the partial pressure of nitrogen (P/P_0), where P is the pressure of nitrogen and P_0 is the saturated vapor pressure of nitrogen at liquid nitrogen temperatures. This method has been widely accepted and employed in various fields (Qiu et al., 2020). The nitrogen adsorption-desorption isotherms for the samples and modified samples are showcased in Figure 8. The synthesized sample presented a type-II curve (as classified by IUPAC) with significant uptakes at low relative pressures ($P/P_0 < 0.1$), implying that the majority of the sample comprises mesopores. The generation of a reversible Type II isotherm is attributed to the physisorption of most gases on non-porous or macroporous adsorbents (Zelenka et al., 2023). The shapes arise from the uncontrolled adsorption of monolayers and multilayers at a high P/P_0 ratio. The initial B-point of the nearly linear center section typically corresponds to the completion of monolayer coverage when the knee is sharp. A more gradual curvature, or a less pronounced Point B, suggests the overlap of monolayer coverage and the beginning of multilayer adsorption (Samal et al., 2022; Zelenka et al., 2023). The thickness of the adsorbed multilayer increases indefinitely when P/P_0 equals 1. The breadth of the isotherms of CBE3 and SBE3 indicated the existence of a wide pore size range. In addition, all the activated materials exhibited capillary condensation with H3-type hysteresis loops at relatively high pressures ($P/P_0 > 0.9$), further indicating mesopore properties. This loop-shaped structure is created by the combination of non-rigid plate-like particles, such as certain clays. However, it may also form if the pore network has macropores that are not filled with pore condensates (Schlumberger and Thommes, 2021).

Table 2 presents the SBET properties, pore volumes, and pore diameters of the PAN/PVDF/SiO_2-CCS samples of SBE3 and CBE3, along with their corresponding high surface areas. The small diameter of the nanofibers was responsible for the increased surface area per unit volume, as demonstrated by the SEM analysis. The study showed that the specific pore volume and BET pore surface area (S_{BET}) increased due to

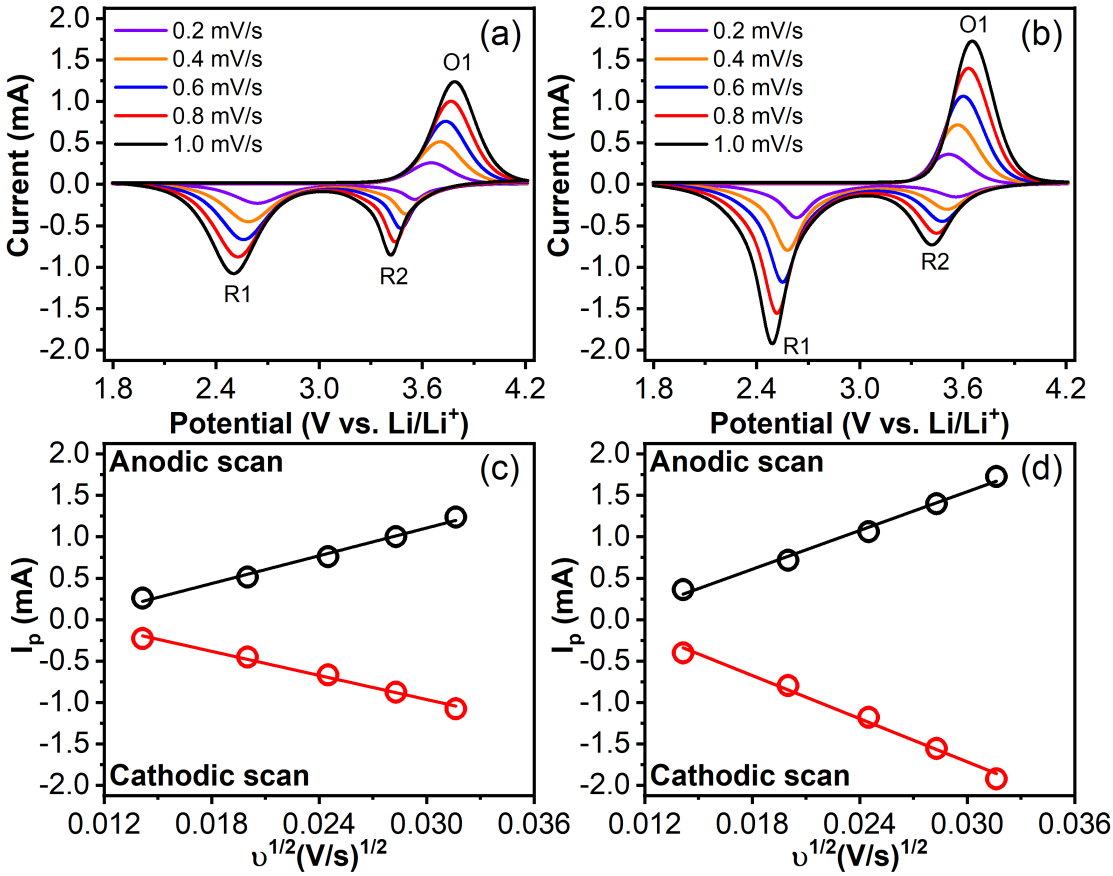

Figure 10. CV Curves Scan Obtained at Various Scan Rates (0.2–1.0 mV/s) in a 1.0 M LiCl Electrolyte Solution for Batteries with (a) SBE and (b) CBE Anodes. Peak Current (ip) vs. the Square Root of the Potential Scanning Rate for the (c) SBE and (d) CBE Anode Scans

Table 2. Surface Area, Pore Size, and Pore Volume of SBE2 and CBE3.

Sample	SBET (m^2/g)	Pore Volume (cm^3/g)	Pore Diameter (nm)
SBE3	31.84	0.37	5.01
CBE3	52.96	0.41	4.52

the dominance of SiO_2 or CCS in the PAN/PVDF polymer matrix. The total pore volume values were 0.37 and 0.41 cm^3/g for SBE3 and CBE3, respectively, and the SBE and CBE values were 31.84 and 52.96 m^2/g, respectively. This is because of the intercalation of larger inorganic/organic cations in the CBE and SBE membrane sheets. At high temperatures, the pore size distribution curve shifts slightly, resulting in more mesopores (2–50 nm). In a previous study involving a cornstalk core anode, SBET was 393.87 m^2/g (Li et al., 2018). In addition, research involving cotton stalk anodes revealed an SBET of 40.19-4173.0 m^2/g (Chang et al., 2022). Both isotherm profiles were classified as Type IV. In addition, nanoparticles from green tea waste-activated carbon exhibited an SBET of 1241 m^2/g, with the isotherm profile indexed as type II (Sankar et al., 2019). This nanopore conductive architecture offers a low-resistance ion diffusion channel and less rapid electron transfer framework. The porous composition of SBE3 and CBE3 nanofibers enhances the electrolyte transport route, thereby decreasing the distance required for lithium ions to diffuse in carbon materials. The presence of these pores reduces the resistance and shortens the path that lithium ions must travel (He et al., 2023; Li et al., 2022). This was further confirmed by the CV and EIS results. However, the pore diameters significantly decrease, when SBE and CBE are 5.01 and 4.52 nm, respectively. This may be due to the pore-blocking effect caused by larger cation/molecule exchanges blocking some of the smaller pores (Cui et al., 2019; Schlumberger and Thommes, 2021). Overall, the tested nanofiber coatings had suitable surface areas for nanofiber anode membrane applications.

3.6 Cyclic Voltammetry (CV)

CV is an electrochemical measurement technique that measures the current response of active solution reduction-oxidation processes at the electrode-solution interface with respect to a

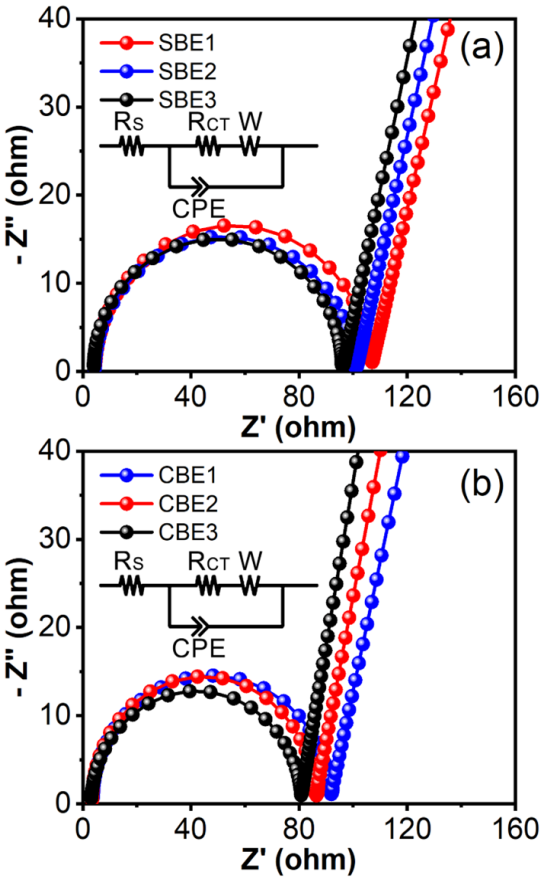

Figure 11. Nyquist Plots of the Electrospun PAN/PVDF/SiO_2-CCS Nanofiber Composites of (a) SBE1 and (b) CBE1, at Frequencies of 10^5~10^2 Hz

linear cyclical potential sweep (Elgrishi et al., 2018). The CV test data are in the form of cyclic voltammogram curves that show the relationship between the voltage (V) as the input and output current (mA). The applied potential was in the range of 1.8–4.2 V, with a scan rate of 1.0 mV/s. Concentration significantly affects the peak position of the electrochemical reaction potential of the battery, as shown in Figure 9. A sharp oxidation peak of high order (O1), obtained around 3.55–3.75 V, can be regarded as an interaction originating from the reduction of SiO_2-CCS into elemental Si/C owing to an alloying reaction between Si/C and Li^+, causing irreversible decomposition of the ferrite starting compound. Two reduction peaks, corresponding to a high order (R1) at around 2.41–2.58 V and low order (R2) at 3.35–3.50 V, were observed during a cathodic scan (Figure 9a). The origin of these peaks was attributed to the decomposition of the electrolyte and the formation of a solid electrolyte interface (SEI) on the electrode surface. The emergence of the two reductive peaks can be attributed to the insertion of Li^+ ions into the incorporated carbon black (Wang et al., 2022c). The potential difference (gap) between the redox peaks in the battery with the CCS (SBE) anode variation (~1.14 V) was lower than that in the battery with the SiO_2 (CBE) anode variation (~0.16 V). The comprehensive reduction and oxidation peak data for battery anode variations are listed in Table 3. CBE demonstrated a considerably greater peak current than SBE, attributable to the higher electrochemical reactivity of CBE electrodes, which was brought about by the exceptional intrinsic ion conductivity of the PAN/PVDF binder and an even dispersion of the active components.

The difference between the current and potential with respect to the number of cycles was insignificant, as shown in Figure 9. The level of potential rose significantly due to the degradation of the electrolyte on the surface of the composite and the formation of an irreversible SEI layer on the electrode surface (Wang et al., 2022c). After the first cycle, this peak was retained, and a stable SEI was formed. The synthesis of elemental Si and some silicates as well as the reduction of SiO_x were responsible for the reduction peak at approximately 2.49 V. Two well-defined peaks were observed in the reduction process, indicating the formation of Li_xSi alloy from lithiated Si (Martín Yerga et al., 2022; Xu et al., 2023). In addition, the intercalation of lithium into a disordered carbon material layer was due to structural defects in some basic planes of the carbon nanosheets in the CCS (Adams et al., 2019). During the anodic cycle, the strength of both oxidation peaks increased, largely owing to the progressive activation of the anode at approximately 3.65 V. The presence of Li^+ in the CCS may result from its interaction with the residual oxygen-containing functional groups. During the anodic cycle, the oxidation peaks exhibited a rise in intensity, which was primarily ascribed to the progressive activation of the anode (Venugopal, 2021). In addition, the reduction and oxidation peak currents observed in CBS3 were higher those observed in SBE, indicating a higher Li insertion capacity. Comprehensive data on the reduction and oxidation peaks versus the cycle number revisions are presented in Table 4. Thus, the battery has superior cycle reversibility, stability, and lower polarization, as evidenced by the smaller peak potential differences and rapidly increasing current.

To better understand the reason why the enhancement of SiO_2 and CCS improves the electrochemical performance, we performed measurements at varying scan rates (0.2–1.0 mV/s) within the potential range of 1.8–4.2. Figure 10a-b show the cyclic voltammogram profiles of the batteries with SBE3 and CBE3 anodes. The reduction and oxidation peaks increased with increasing scan speed because dividing the peak area by the scan speed resulted in a constant electrode capacity. The exceptionally symmetrical peaks demonstrate the remarkable cyclic reversibility and stability of the lithium insertion and extraction processes (Zhang et al., 2022b). The root cause of this issue can be traced back to the insufficient extraction or insertion of ions between the Si and C elements during the conversion process, especially when high-speed scanning is involved, which may result in irreversible behavior. Moreover, the diffusion-controlled mechanism for the entire electrode reaction and the customary equilibrium behavior of intercalation-type electrodes were demonstrated through a strong linear correlation (Venugopal, 2021). If charge transfer at the interface is suf-

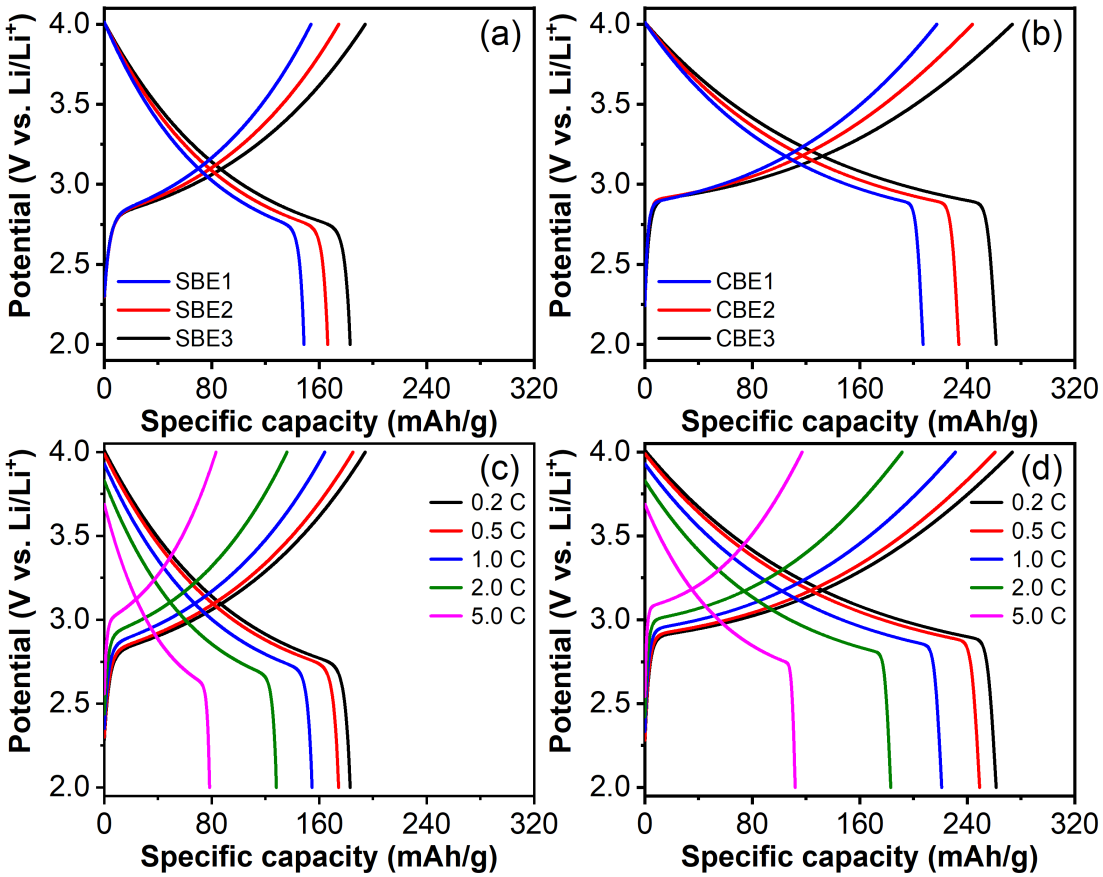

Figure 12. Electrochemical Measurement of Nanofiber Composite Anode for Initial Charge-Discharge Profiles. Concentration Variation: (a) SBE and (b) CSS. Scan Rate Variation: (a) SBE3 and (b) CSS3

ficiently fast, the diffusion of ions in the electrode should be considered the rate-limiting step; therefore, the diffusing ability of ions should be investigated. The Randles–Sevcik plot of the material is shown in Figure 10c-d where the diffusion coefficient of lithium ions can be determined from the anodic peak Ipa (mA). The cathodic peak Ipc (mA), calculated as a function of the square root of the scanning speed $v^{1/2}$ $(V/s)^{1/2}$, increases with the scanning speed (Feng et al., 2017; Rahman et al., 2019).

$$I_p = (2.69 \times 10^5) n^{3/2} A D_{Li^+}^{1/2} C_{Li} v^{1/2} \quad (1)$$

The diffusion coefficient of lithium ions was determined using Equation 1, where n is the number of electrons transferred per mole (n = 1), C (mol/cm^3) is the concentration of Li in the electrode (0.03), and D_{Li}^+ (cm^2/s) is the Li diffusion coefficient (Feng et al., 2017). A (cm^2) represents the electrode areas set for SBE3 and CBE3, which are 31.84 and 52.96 m^2/g, respectively. Each electrode weighed 9 mg. The calculated D_{Li}^+ values for the SBE3 and CBE3 electrodes during cathodic scanning were 1.13×10^{-12} and 1.21×10^{-12} cm^2/s, respectively. In the anodic scan, the D_{Li}^+ values of the two electrodes were 1.09×10^{-12} and 1.30×10^{-12} cm^2/s, respectively. During charging and discharging, the CBE3 electrode showed a slightly higher D_{Li}^+ than the SBE3 electrode. In addition, the peak O1 had a larger diffusion coefficient than the peak R1 during the extraction process, confirming that the kinetic extraction of alkali ions was the most difficult and consumed the most energy (Martín Yerga et al., 2022). This confirms that the Li^+ ions exhibit excellent transmission performance, indicating excellent electrochemical performance in our Li-ion batteries.

3.7 Electrochemical Impedance Spectroscopy (EIS)

Electrochemical Impedance Spectroscopy (EIS) is a method used to evaluate the response of a system to a disturbance in its steady state by applying a small-amplitude voltage or current to the electrodes (Jauhari et al., 2021; Loghavi et al., 2020). EIS was employed to examine the electrochemical behavior of six samples, consisting of three each of SBE and CBE. The Nyquist plots depicted a semicircle in the high-frequency region and a sloping line, as illustrated in Figure 11. he impedance values were analyzed using an equivalent circuit model, and the results are presented in Table 5 The diffusion resistance (RS) of lithium ions through the SEI layer, obtained by equivalent circuit truncation, characterizes the transport of lithium ions

Table 3. Reduction and Oxidation Peaks for Various Battery Anode Configurations

Sample	I_{O1} (mA)	V_{O1} (V)	I_{R1} (mA)	V_{R1} (V)	I_{R2} (mA)	V_{R2} (V)	ΔV (V)
SBE1	1.238	3.788	1.076	2.502	0.613	3.371	1.286
SBE2	1.358	3.755	1.124	2.510	0.546	3.413	1.245
SBE3	1.517	3.716	1.241	2.574	0.503	3.466	1.142
CBE1	1.502	3.618	1.636	2.497	0.627	3.423	1.121
CBE2	1.593	3.632	1.772	2.527	0.674	3.422	1.105
CBE3	1.728	3.653	1.921	2.492	0.731	3.419	1.162

Table 4. Reduction and Oxidation Peaks for Variations in the Cyclic Number

Sample	I_{O1} (mA)	V_{O1} (V)	I_{R1} (mA)	V_{R1} (V)	I_{R2} (mA)	V_{R2} (V)	ΔV (V)
SBE3	1	1.238	3.788	1.076	2.502	0.853	3.416
	3	1.280	3.793	1.113	2.497	0.882	3.411
	5	1.322	3.798	1.149	2.492	0.911	3.406
SBE3	1	1.728	3.653	1.921	2.492	0.731	3.412
	3	1.783	3.658	1.983	2.487	0.755	3.414
	5	1.838	3.664	2.044	2.482	0.778	3.409

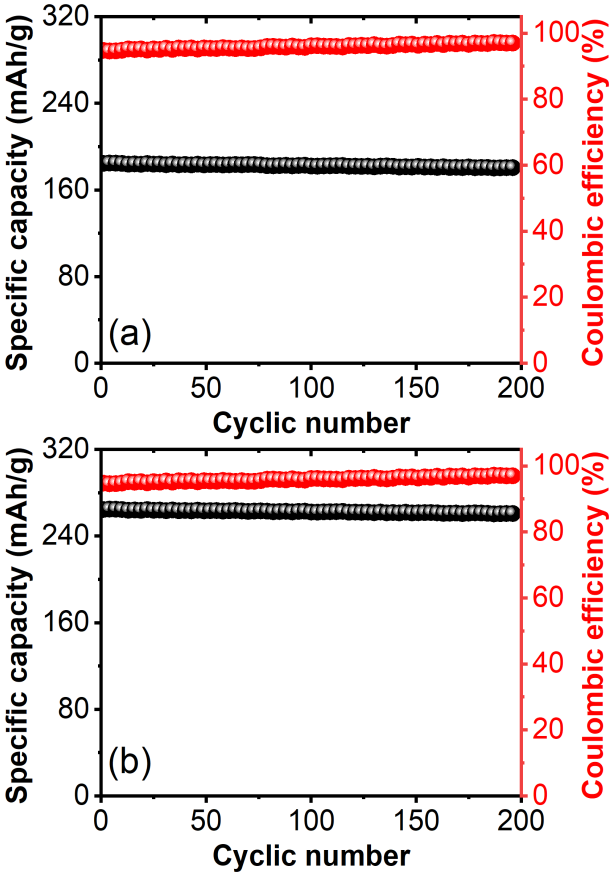

Figure 13. Rate Capabilities of (a) SBE3 and (b) CSS3 Batteries

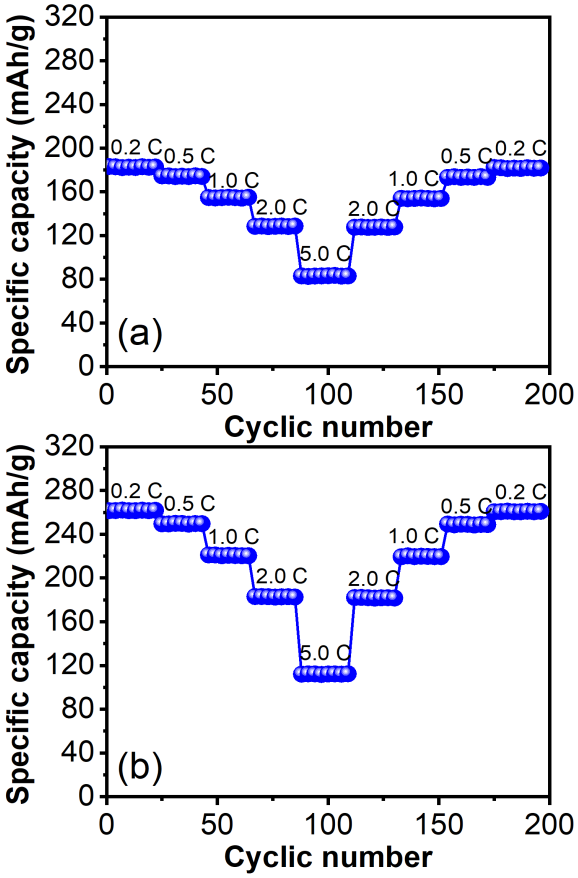

Figure 14. Cycling Performance of (a) SBE3 and (b) CSS3 Batteries.

Table 5. Resistance Values Obtained by Fitting the Impedance Spectra

Sample	R_S (ohm)	R_{CT} (ohm)	W (Warburg resistance)
SBE1	4.04	92.27	0.710
SBE2	4.33	96.76	0.550
SBE3	4.57	102.45	1.256
CBE1	3.67	88.52	1.420
CBE2	3.38	83.03	1.100
CBE3	3.12	77.64	2.512

in the bulk phase of the liquid electrolyte (Gao et al., 2019). Owing to the conductive nanofiber structure, an appropriate Li^+ diffusion rate and high electrical conductivity resulted in outstanding performance (Belgibayeva and Taniguchi, 2021; Liu et al., 2022). The outcomes were in line with the findings of previous studies that examined CV diffusion. The presence of large-sized particles in SBE and CBE hinders the diffusion of lithium-ion at high current intensities, as indicated by the low-frequency region revealed by the EIS test (Cao et al., 2020). The highest diffusion resistance due to SiO_2 variation was observed in SBE3, while CBE3 displayed the highest resistance due to CCS variation.

The Warburg resistance, also known as the straight line at low frequencies, is a measure of ion diffusion within the electrode. It is considered to be the low-frequency resistance and is a key parameter for understanding electrochemical impedance. The Warburg resistance originates from the diffusion process, and its effect is prominent at low frequencies and negligible at high frequencies (Belgibayeva and Taniguchi, 2021; Liu et al., 2022). The Warburg resistance in the LiCl electrolyte was minimal because of diffusion-controlled reactions, as confirmed by the CV curves. Charges primarily accumulate on the surface via the formation of a double layer, which offers maximum resistance to diffusion-controlled processes. The low-frequency region, attributed to the charge transfer resistance (RCT) due to phase-crossing ionic transfer processes, characterizes the polarization resistance of the porous electrodes (Gao et al., 2019). The RCT of the PI separator constructed decreased in the following sequence: SBE1<SBE2<SBE3, and CBE1<CBE2<CBE3. A reduction in porosity of the membrane was observed with increased concentrations of SiO_2 and CCS, while surface polarity increased. In other words, the excellent polarity of the used electrode compensates, to some extent, for the higher interfacial resistance caused by the lower electrode porosity (Belgibayeva and Taniguchi, 2021). The polarity of the electrode surface increased, but the porosity was not significantly reduced, resulting in the lowest interfacial impedance. Owing to its low surface polarity and porosity, the interfacial impedance of the electrode was likely to be greater for CBE1 than for SBE1. The improved charge/discharge process and enhanced electrochemical performance were made possible by the reduction in charge transfer and ion diffusion resistances, which facilitated the kinetic behavior (Jauhari et al., 2021; Loghavi et al., 2020).

3.8 Charge–Discharge Performance

Charge–discharge performance is often used to evaluate energy storage systems and materials (Wu et al., 2021; Zhang et al., 2022b). The behavior of the charge-discharge process at room temperature, as illustrated in Figure 12a-b, was examined using a galvanostatic protocol at a rate of 1 C per hour in the voltage range of 2.7-4.2 V. All samples demonstrated a nearly constant voltage of approximately 3.45 V, corresponding to the Li^+ insertion and extraction processes. The specific discharge capacities for SBE1, SBE2, and SBE3 were 148.72, 166.31, and 183.14 mAh/g, respectively, while the specific discharge capacities for SBE1, SBE2, and SBE3 were 261.52, 233.71, and 207.13 mAh/g, respectively. The increase in capacity can be attributed to the presence of the carbon layer, which enhanced the electrical conductivity. In addition, the sample uniformly attached SiO_2 and CCS to the polymer, resulting in improved electrical conductivity through the formation of a wide range of conductive networks. The reduced SBE and CBE voltages demonstrated lower levels of polarization during the charge-discharge cycle, likely due to the promoted diffusion of lithium ions and improved electronic conductivity of the porous SBE and CBE composite microspheres. This can be used to explain the incorporation of ions into the lithium-ion system owing to the voltage difference (Belgibayeva and Taniguchi, 2021). Dominant Li^+ insertion is preferred, mainly because of the relaxation characteristics of Li^+. When Li^+ ions enter a site in a stepwise manner, the entire configuration is likely to undergo a related reorganization to a stable state, and different entry voltage plateaus result from structural reorganization, reduction, and oxidation transformations (Venugopal, 2021; Zhang et al., 2022b). Figure 12b-c show the discharge curves at various rates (0.2–5.0 C) in the range of 2.7–4.2 V. As expected, the charging rate was almost equal to the discharge rate. The specific capacity decreases as the C-rate increases. The specific discharge capacities of SBE1–SBE3 were 183.1, 174.5, 154.7, 128.1, and 78.4 mAh/g. The specific discharge capacities of CBE1–CBE3 were 261.5, 249.2, 220.9, 183.1, and 111.9 mAh/g. The gradual incline might be attributable to the capacitive nature of the lithium storage process at the interface, which is analogous to the behavior observed in nano-sized transition metal oxides at low voltage levels (Keppeler and Srinivasan, 2017). The connection between the tip slope region and interfacial ion storage is established. In nanoscale active materials, a pseudocapacitive effect may emerge at the surface, resulting in a combined total charge storage that consists of lithium-ion intercalation and capacitive behavior. This has been previously documented for hierarchically constructed nanoplates. The use of American English, with its specific terms and phrases, is strictly adhered to in generating the desired outcome (Han et al., 2021). According to this study, it is clear that SiO_2 and CSS bonded to a polymer matrix can

enhance the Li-ion storage capacity in anode materials.

The long-term stability of the cycle was assessed using galvanostatic charge-discharge tests within a voltage range of 0.2–5.0 V. However, the SBE demonstrated expected stability with minimal capacity degradation after 200 cycles at a rate of 5 C. In comparison, the system provided a significantly lower capacity than CBE at the same rate (a shown in Figure 13). The discharge-specific capacities at the initial cycle were 184.51 and 264.57 mAh/g for the SBE and CBE electrodes, respectively. The initial Coulombic efficiency was 96.2%, and the average efficiency from cycles 2 to 200 was 94.4%. The irreversible initial cycling capacity can be attributed to electrolyte reduction, which leads to the formation of a SEI on the surface of the active particles due to irreversible lithium insertion into the nanocomposite (Liu et al., 2022; Xu et al., 2023), However, during the 52nd cycle, the capacitance dropped significantly to 183.35 and 263.47 milliampere hours per gram (mAh/g) for SBE3 and CBE3 electrodes, respectively. Despite the decrease in performance, the two electrodes continued to display high reversible capacities after 200 cycles. Specifically, the electrode with 180.56 mAh/g capacity and the electrode with 260.86 mAh/g capacity showed impressive results. The presence of the SiO_2 layer and carbon network was critical to the improved lithium storage properties of the nanocomposite electrodes. This buffer layer provided uninterrupted mechanical support during the charge/discharge processes, significantly contributing to the overall performance of the electrodes (Sui et al., 2023).

To assess the rate capability, the researchers performed charge-discharge tests at various current densities ranging from 0.2 to 1.0 C. As illustrated in Figure 14, the discharge capacity of SiO_2-C changed according to the current density, decreasing from 183.15 to 182.86, 174.59, 154.76, 128.40, and finally 83.06 mA/g. Additionally, after numerous rate cycles, the reversible capacity returned to 127.60 mAh/g when the current density was reduced to 0.2 C, and to 196 mAh/g at a density of 0.2 C, which is consistent with the findings of Triwibowo et al. (2016), who were able to maintain a capacitance of 93.54 with a retention rate of 94.99% for carbon-coated $LiFePO_4$. Furthermore, the capacity values of SBE3 and CBE3 were lower than that of an Mo doped MnO_2 material in research by Xia et al. (2020), with the capacitance ranging from 476.8–802.9 mAh/g. However, SBE3 and CBE3 had higher values than that of the nanoscale $LiFePO_4$ material in the research of Cheng et al. (2017), with a capacitance ranging from 40–160 mAh/g. The SiO_2-C composite demonstrated exceptional stability, even at extremely high current densities, attributed to the presence of a SiO_2 layer and carbon matrix coating on its surface. These components provided effective cushioning and significantly improved electrical conductivity at high current densities (Al Ja'farawy et al., 2021; Belgibayeva and Taniguchi, 2019). The carbon matrix not only facilitated the adsorption of Li ions but also acted as a swift conduit for electron and Li ion transport, leading to exceptional electrical conductivity and Li-ion diffusion during discharge-charge cycles. Furthermore, the high capacity is likely attributed to the high specific surface area, and the graphite structure provides additional lithium-ion storage sites beyond the conventional graphite intercalation mechanism (Hu et al., 2021). Lithium ions can be electrochemically absorbed and inserted into both the surface and the micro/mesopores of a disordered carbon layer, leading to an increased reversible storage capacity for Li^+.

4. CONCLUSIONS

The PAN/PVDF composite nanofiber structure incorporating SiO_2/CCS presents several benefits for use as an anode material in lithium-ion batteries. Carbon materials derived from biomass are highly sought-after as anodes in lithium-ion batteries due to their low cost and superior performance. The addition of SiO_2 to carbon improved the structural stability and electrochemical reaction kinematics of the resulting nanofibers. The diameters of the nanofibers ranged from 575–707 nm, and their mechanical strengths were 13.7±0.4 MPa, 34.4±0.1 MPa, and 982 ± 109 kJ/m^3, respectively. CV revealed a potential difference of less than 1.286 V in the first cycle, which remained below 3.416 V in the second and third cycles, with a lithium-ion diffusion coefficient below 4.73×10^{13} cm^2/s. After conducting 200 cycles, the nanofiber demonstrated an impressive capacity of 382 mhA/g while maintaining 98% stability. These results suggest that the PAN/PVDF/SiO_2-CCS composite membrane is a promising candidate for use as an anode material in lithium-ion batteries.

5. ACKNOWLEDGMENT

This study was funded by DIPA of the Public Service Agency of Universitas Sriwijaya, 2023. SP DIPA-123.17.2.677515 /2023, on November 30, 2022. Rector's decree number: 0187/UN9.3.1/SK/2023 dated April 18, 2023.

REFERENCES

Adams, R. A., A. Varma, and V. G. Pol (2019). Carbon Anodes for Nonaqueous Alkali Metal-Ion Batteries and Their Thermal Safety Aspects. *Advanced Energy Materials*, **9**(35); 1900550

Aghayari, S. (2022). PVDF Composite Nanofibers Applications. *Heliyon*, **8**(11); e11260

Al Ja'farawy, M. S., D. N. Hikmah, U. Riyadi, A. Purwanto, and H. Widiyandari (2021). A Review: The Development of SiO_2/C Anode Materials for Lithium-Ion Batteries. *Journal of Electronic Materials*, **50**(12); 1–21

Almafie, M. R., L. Marlina, R. Riyanto, J. Jauhari, Z. Nawawi, and I. Sriyanti (2022). Dielectric Properties and Flexibility of Polyacrylonitrile/Graphene Oxide Composite Nanofibers. *ACS omega*, **7**(37); 33087–33096

Anuchi, S. O., K. L. S. Campbell, and J. P. Hallett (2022). Effective Pretreatment of Lignin-Rich Coconut Wastes Using a Low-Cost Ionic Liquid. *Scientific Reports*, **12**(1); 6108

Awadh, S. M. and Z. M. Yaseen (2019). Investigation of Silica Polymorphs Stratified in Siliceous Geode Using FTIR and XRD Methods. *Materials Chemistry and Physics*, **228**; 45–50

Bag, O., K. Tekin, and S. Karagoz (2020). Microporous Activated Carbons from Lignocellulosic Biomass by KOH Activation. *Fullerenes, Nanotubes and Carbon Nanostructures*, **28**(12); 1030–1037

Belgibayeva, A. and I. Taniguchi (2019). Synthesis and Characterization of SiO_2/C Composite Nanofibers As Free-Standing Anode Materials for Li-Ion Batteries. *Electrochimica Acta*, **328**; 135101

Belgibayeva, A. and I. Taniguchi (2021). Insights into the Improved Electrochemical Performance of Lithium-Sulfur Battery with Free-Standing SiO_2/C Composite Nanofiber Mat Interlayer. *Journal of Power Sources*, **484**; 229308

Cao, X., C. Ma, L. Luo, L. Chen, H. Cheng, R. S. Orenstein, and X. Zhang (2023). Nanofiber Materials for Lithium-Ion Batteries. *Advanced Fiber Materials*, **5**(4); 1141–1197

Cao, Z., M. Sang, S. Chen, J. Jia, M. Yang, H. Zhang, X. Li, and S. Yang (2020). *In situ* Constructed (010)-Oriented $LiFePO_4$ Nanocrystals/Carbon Nanofiber Hybrid Network: Facile Synthesis of Free-Standing Cathodes for Lithium-Ion Batteries. *Electrochimica Acta*, **333**; 135538

Chang, H., H. Deng, Y. Wang, S. Wang, L. Cao, Z. Dong, and T. Tan (2022). Synthesis of Large Mesoporous Carbon from Cotton Stalk for Use As an Anode for Lithium-Ion Batteries. *Biomass and Bioenergy*, **167**; 106641

Chen, Q., L. Tan, S. Wang, B. Liu, Q. Peng, H. Luo, P. Jiang, H. Tang, and R. Sun (2021). A Facile Synthesis of Phosphorus Doped Si/SiO_2/C with High Coulombic Efficiency and Good Stability As an Anode Material for Lithium Ion Batteries. *Electrochimica Acta*, **385**; 138385

Cheng, W. h., L. Wang, Q. b. Zhang, Z. j. Wang, J. b. Xu, W. Ren, L. Bian, and A. m. Chang (2017). Preparation and Characterization of Nanoscale $LiFePO_4$ Cathode Materials by a Two-Step Solid-State Reaction Method. *Journal of Materials Science*, **52**; 2366–2372

Cui, M., L. Wang, X. Guo, E. Wang, Y. Yang, T. Wu, D. He, S. Liu, and H. Yu (2019). Designing of Hierarchical Mesoporous/macroporous Silicon-Based Composite Anode Material for Low-Cost High-Performance Lithium-Ion Batteries. *Journal of Materials Chemistry A*, **7**(8); 3874–3881

Da Róz, A., F. Leite, L. Pereiro, P. Nascente, V. Zucolotto, O. Oliveira Jr, and A. Carvalho (2010). Adsorption of Chitosan on Spin-Coated Cellulose Films. *Carbohydrate Polymers*, **80**(1); 65–70

Darmawan, S., L. Efiyanti, N. Saputra, H. Wibisono, G. Pari, D. Hendra, J. Adam, and Mufti (2022). Quality of Microporous Activated Charcoal from Coconut Shell Waste in Industrial Scale. *Asian Journal of Chemistry*, **34**; 543–549

Descals, A., S. Wich, E. Meijaard, D. L. Gaveau, S. Peedell, and Z. Szantoi (2020). High-Resolution Global Map of Smallholder and Industrial Closed-Canopy Oil Palm Plantations. *Earth System Science Data Discussions*, **2020**(3); 1–22

Duan, D., D. Chen, L. Huang, Y. Zhang, Y. Zhang, Q. Wang, G. Xiao, W. Zhang, H. Lei, and R. Ruan (2021). Activated Carbon from Lignocellulosic Biomass As Catalyst: A Review of the Applications in Fast Pyrolysis Process. *Journal of Analytical and Applied Pyrolysis*, **158**; 105246

El Sakhawy, M., S. Kamel, A. Salama, and H. A. S. Tohamy (2018). Preparation and Infrared Study of Cellulose Based Amphiphilic Materials. *Cellulose Chemistry and Technology*, **52**(3-4); 193–200

Elele, E., Y. Shen, J. Tang, Q. Lei, B. Khusid, G. Tkacik, and C. Carbrello (2019). Mechanical Properties of Polymeric Microfiltration Membranes. *Journal of Membrane Science*, **591**; 117351

Elgrishi, N., K. J. Rountree, B. D. McCarthy, E. S. Rountree, T. T. Eisenhart, and J. L. Dempsey (2018). A Practical Beginner's Guide to Cyclic Voltammetry. *Journal of Chemical Education*, **95**(2); 197–206

Ellerbrock, R., M. Stein, and J. Schaller (2022). Comparing Amorphous Silica, Short-Range-Ordered Silicates and Silicic Acid Species by FTIR. *Scientific Reports*, **12**(1); 11708

Fatmawati, A., T. Nurtono, and A. Widjaja (2023). Thermogravimetric Kinetic-Based Computation of Raw and Pretreated Coconut Husk Powder Lignocellulosic Composition. *Bioresource Technology Reports*, **22**; 101500

Feng, X. Y., X. Li, M. Tang, A. Gan, and Y. Y. Hu (2017). Enhanced Rate Performance of $Li_4Ti_5O_{12}$ Anodes with Bridged Grain Boundaries. *Journal of Power Sources*, **354**; 172–178

Figueroa Campos, G. A., J. P. H. Perez, I. Block, S. T. Sagu, P. Saravia Celis, A. Taubert, and H. M. Rawel (2021). Preparation of Activated Carbons from Spent Coffee Grounds and Coffee Parchment and Assessment of Their Adsorbent Efficiency. *Processes*, **9**(8); 1396

Gao, X., L. Sheng, L. Yang, X. Xie, D. Li, Y. Gong, M. Cao, Y. Bai, H. Dong, and G. Liu (2023). High-Stability Core-Shell Structured PAN/PVDF Nanofiber Separator with Excellent Lithium-Ion Transport Property for Lithium-Based Battery. *Journal of Colloid and Interface Science*, **636**; 317–327

Gao, Y., Z. Pan, J. Sun, Z. Liu, and J. Wang (2022). High-Energy Batteries: Beyond Lithium-Ion and Their Long Road to Commercialisation. *Nano-Micro Letters*, **14**(1); 94

Gao, Y., L. Yin, S. J. Kim, H. Yang, I. Jeon, J. P. Kim, S. Y. Jeong, H. W. Lee, and C. R. Cho (2019). Enhanced Lithium Storage by $ZnFe_2O_4$ Nanofibers As Anode Materials for Lithium-Ion Battery. *Electrochimica Acta*, **296**; 565–574

Gong, W., J. Gu, S. Ruan, and C. Shen (2019). Preparation of High-Strength Polyvinylidene Fluoride Lithium-Ion Battery Separator by Electrospinning. *Gaofenzi Cailiao Kexue Yu Gongcheng/Polymeric Materials Science and Engineering*, **35**(3); 148–155

Gonzalez, I. Z., H. C. Chiu, R. Gauvin, G. P. Demopoulos, and Y. Verde Gomez (2022). Silicon Doped Carbon Nanotubes As High Energy Anode for Lithium-Ion Batteries. *Materials Today Communications*, **30**; 103158

Han, X., Q. Meng, X. Wan, B. Sun, Y. Zhang, B. Shen, J. Gao, Y. Ma, P. Zuo, and S. Lou (2021). Intercalation

Pseudocapacitive Electrochemistry of Nb-Based Oxides for Fast Charging of Lithium-Ion Batteries. *Nano Energy*, **81**; 105635

He, J., J. Meng, and Y. Huang (2023). Challenges and Recent Progress in Fast-Charging Lithium-Ion Battery Materials. *Journal of Power Sources*, **570**; 232965

Hu, D., L. Chen, J. Tian, Y. Su, N. Li, G. Chen, Y. Hu, Y. Dou, S. Chen, and F. Wu (2021). Research Progress of Lithium Plating on Graphite Anode in Lithium-Ion Batteries. *Chinese Journal of Chemistry*, **39**(1); 165–173

Hu, X. and Z. Lin (2021). Transforming Waste Polypropylene Face Masks into S-Doped Porous Carbon As the Cathode Electrode for Supercapacitors. *Ionics*, **27**(5); 2169–2179

Jauhari, J., M. R. Almafie, L. Marlina, Z. Nawawi, and I. Sriyanti (2021). Physicochemical Properties and Performance of Graphene Oxide/Polyacrylonitrile Composite Fibers As Supercapacitor Electrode Materials. *RSC advances*, **11**(19); 11233–11243

Kalu Uka, G. M., S. Kumar, A. C. Kalu Uka, S. Vikram, G. O. Ihekweme, N. Ranjan, E. N. Anosike Francis, G. Prajapati, A. Nduba, and A. P. Onwualu (2022). Production of Activated Carbon Electrode for Energy Storage Application in Supercapacitors Via KOH Activation of Waste Termite Biomass. *Waste and Biomass Valorization*, **13**(5); 1–16

Kanjana, K., P. Harding, T. Kwamman, W. Kingkam, and T. Chutimasakul (2021). Biomass-Derived Activated Carbons with Extremely Narrow Pore Size Distribution Via Eco-Friendly Synthesis for Supercapacitor Application. *Biomass and Bioenergy*, **153**; 106206

Keppeler, M. and M. Srinivasan (2017). Interfacial Phenomena/Capacities Beyond Conversion Reaction Occurring in Nano-sized Transition-Metal-Oxide-Based Negative Electrodes in Lithium-Ion Batteries: A Review. *ChemElectroChem*, **4**(11); 2727–2754

Keppetipola, N. M., M. Dissanayake, P. Dissanayake, B. Karunarathne, M. A. Dourges, D. Talaga, L. Servant, C. Olivier, T. Toupance, and S. Uchida (2021). Graphite-Type Activated Carbon from Coconut Shell: A Natural Source for Eco-Friendly Non-Volatile Storage Devices. *RSC Advances*, **11**(5); 2854–2865

Khan, A., A. M. Asiri, M. Jawaid, and N. Saba (2020). Effect of Cellulose Nano Fibers and Nano Clays on the Mechanical, Morphological, Thermal and Dynamic Mechanical Performance of Kenaf/Epoxy Composites. *Carbohydrate Polymers*, **239**; 116248

Khoshnood Motlagh, E., N. Asasian Kolur, and S. Sharifian (2022). A Comparative Study on Rice Husk and Rice Straw As Bioresources for Production of Carbonaceous Adsorbent and Silica. *Biomass Conversion and Biorefinery*, **12**(12); 5729–5738

Lee, J. H., M. G. T. Nathan, H. W. Kim, S. M. Lee, H. I. Kim, J. H. Kim, I. Seo, and J. K. Kim (2022). A High-Stable Polyacrylonitrile/Ceramic Composite Membranes for High-Voltage Lithium-Ion Batteries. *Materials Chemistry and Physics*, **291**; 126516

Li, S., K. Wang, G. Zhang, S. Li, Y. Xu, X. Zhang, X. Zhang, S. Zheng, X. Sun, and Y. Ma (2022). Fast Charging Anode Materials for Lithium-Ion Batteries: Current Status and Perspectives. *Advanced Functional Materials*, **32**(23); 2200796

Li, Y., C. Li, H. Qi, K. Yu, and C. Liang (2018). Mesoporous Activated Carbon from Corn Stalk Core for Lithium Ion Batteries. *Chemical Physics*, **506**; 10–16

Liu, J., F. Song, Q. Li, J. Li, Z. Hong, C. Wang, M. Liu, L. Bai, and F. Zeng (2021a). Preparation and Performance of Porous Polyethersulfone (PES)/Al_2O_3 Separator for High-Performance Lithium-Oxygen Battery. *Ionics*, **27**(12); 1–10

Liu, T., Y. Qu, J. Liu, L. Zhang, B. Cheng, and J. Yu (2021b). Core-Shell Structured C@SiO_2 Hollow Spheres Decorated with Nickel Nanoparticles As Anode Materials for Lithium-Ion Batteries. *Small*, **17**(49); 2103673

Liu, X., J. Zhao, J. Wang, Z. Le, P. Nie, H. Wang, T. Xu, G. Xu, L. Chang, and M. Zhu (2022). Papers Electrolyte-Philic and Thermal-Resistant Polyimide Separator Enhances the Performance of Flexible Silicon/carbon Nanofibers for Lithium-Ion Batteries. *Journal of Energy Storage*, **54**; 10532

Liu, Z., G. Li, Q. Qin, L. Mi, G. Li, G. Zheng, C. Liu, Q. Li, and X. Liu (2021c). Electrospun PVDF/PANN Membrane for Pressure Sensor and Sodium-Ion Battery Separator. *Advanced Composites and Hybrid Materials*, **4**(4); 1215–1225

Loghavi, M. M., S. Bahadorikhalili, N. Lari, M. H. Moghim, M. Babaiee, and R. Eqra (2020). The Effect of Crystalline Microstructure of PVDF Binder on Mechanical and Electrochemical Performance of Lithium-Ion Batteries Cathode. *Zeitschrift für Physikalische Chemie*, **234**(3); 381–397

Marques, A., H. Nijveen, C. Somi, W. Ligterink, and H. Hilhorst (2019). Induction of Desiccation Tolerance in Desiccation Sensitive Citrus Limon Seeds. *Journal of Integrative Plant Biology*, **61**(5); 624–638

Martín Yerga, D., D. C. Milan, X. Xu, J. Fernández Vidal, L. Whalley, A. J. Cowan, L. J. Hardwick, and P. R. Unwin (2022). Dynamics of Solid-Electrolyte Interphase Formation on Silicon Electrodes Revealed by Combinatorial Electrochemical Screening. *Angewandte Chemie International Edition*, **61**(34); e202207184

Medhat, A., H. H. El Maghrabi, A. Abdelghany, N. M. A. Menem, P. Raynaud, Y. M. Moustafa, M. A. Elsayed, and A. A. Nada (2021). Efficiently Activated Carbons from Corn Cob for Methylene Blue Adsorption. *Applied Surface Science Advances*, **3**; 100037

Megahed, M., D. Tobbala, and M. A. El baky (2021). The Effect of Incorporation of Hybrid Silica and Cobalt Ferrite Nanofillers on the Mechanical Characteristics of Glass Fiber-Reinforced Polymeric Composites. *Polymer Composites*, **42**(1); 271–284

Méndez, A., M. Álvarez, J. Fidalgo, C. Di Stasi, J. Manyà, and G. Gascó (2022). Biomass-Derived Activated Carbon As Catalyst in the Leaching of Metals from a Copper Sulfide Concentrate. *Minerals Engineering*, **183**; 107594

Moghim, M. H., A. Nahvibayani, and R. Eqra (2022). Mechanical Properties of Heat-Treated Polypropylene Separators

for Lithium-Ion Batteries. *Polymer Engineering & Science*, **62**(9); 3049–3058

Mohammed, Y. A., F. Ma, L. Liu, C. Zhang, H. Dong, Q. Wang, X. Xu, and A. A. Al Wahbi (2021). Preparation of Electrospun Polyvinylidene Fluoride/Amidoximized Polyacrylonitrile Nanofibers for Trace Metal Ions Removal from Contaminated Water. *Journal of Porous Materials*, **28**; 383–392

Nasser, J., L. Zhang, J. Lin, and H. Sodano (2020). Aramid Nanofiber Reinforced Polymer Nanocomposites Via Amide-Amide Hydrogen Bonding. *ACS Applied Polymer Materials*, **2**(7); 2934–2945

Nizam, N. U. M., M. M. Hanafiah, E. Mahmoudi, A. A. Halim, and A. W. Mohammad (2021). The Removal of Anionic and Cationic Dyes from an Aqueous Solution Using Biomass-Based Activated Carbon. *Scientific Reports*, **11**(1); 1–17

Nzereogu, P., A. Omah, F. Ezema, E. Iwuoha, and A. Nwanya (2022). Anode Materials for Lithium-Ion Batteries: A Review. *Applied Surface Science Advances*, **9**; 100233

Qiu, H., L. Zhao, M. Asif, X. Huang, T. Tang, W. Li, T. Zhang, T. Shen, and Y. Hou (2020). SnO_2 Nanoparticles Anchored on Carbon Foam As a Freestanding Anode for High Performance Potassium-Ion Batteries. *Energy & Environmental Science*, **13**(2); 571–578

Rahman, M. M., S. Mateti, Q. Cai, I. Sultana, Y. Fan, X. Wang, C. Hou, and Y. Chen (2019). High Temperature and High Rate Lithium-Ion Batteries with Boron Nitride Nanotubes Coated Polypropylene Separators. *Energy Storage Materials*, **19**; 352–359

Rashid, T. U., R. E. Gorga, and W. E. Krause (2021). Mechanical Properties of Electrospun Fibers—A Critical Review. *Advanced Engineering Materials*, **23**(9); 2100153

Renman, V., M. V. Blanco, A. N. Norberg, F. Vullum Bruer, and A. M. Svensson (2021). Electrochemical Activation of a Diatom-Derived SiO_2/C Composite Anode and Its Implementation in a Lithium Ion Battery. *Solid State Ionics*, **371**; 115766

Rethinam, P. and V. Krishnakumar (2022). Global Scenario of Coconut and Coconut Water. In *Coconut Water: A Promising Natural Health Drink-Distribution, Processing and Nutritional Benefits*. Springer, pages 17–35

Rey, I., C. Vallejo, G. Santiago, M. Iturrondobeitia, and E. Lizundia (2021). Environmental Impacts of Graphite Recycling from Spent Lithium-Ion Batteries Based on Life Cycle Assessment. *ACS Sustainable Chemistry & Engineering*, **9**(43); 14488–14501

Rodrigues, D. L. C., F. M. Machado, A. G. Osório, C. F. de Azevedo, E. C. Lima, R. S. da Silva, D. R. Lima, and F. M. Gonçalves (2020). Adsorption of Amoxicillin onto High Surface Area–Activated Carbons Based on Olive Biomass: Kinetic and Equilibrium Studies. *Environmental Science and Pollution Research*, **27**(33); 41394–41404

Samal, R., S. Radhakrishnan, and C. S. Rout (2022). *Advanced Analytical Techniques for Characterization of 2D Materials*. AIP Publishing LLC

Sankar, S., S. Saravanan, A. T. A. Ahmed, A. I. Inamdar, H. Im, S. Lee, and D. Y. Kim (2019). Spherical Activated-Carbon Nanoparticles Derived from Biomass Green Tea Wastes for Anode Material of Lithium-Ion Battery. *Materials Letters*, **240**; 189–192

Schlumberger, C. and M. Thommes (2021). Characterization of Hierarchically Ordered Porous Materials by Physisorption and Mercury Porosimetry—A Tutorial Review. *Advanced Materials Interfaces*, **8**(4); 2002181

Shafizadeh, A., H. Rastegari, H. Shahbeik, H. Mobli, J. Pan, W. Peng, G. Li, M. Tabatabaei, and M. Aghbashlo (2023). A Critical Review of the Use of Nanomaterials in the Biomass Pyrolysis Process. *Journal of Cleaner Production*, **400**; 136705

Si, L., K. Yan, C. Li, Y. Huang, X. Pang, X. Yang, D. Sui, Y. Zhang, J. Wang, and C. C. Xu (2022). Binder-Free SiO_2 Nanotubes/Carbon Nanofibers Mat As Superior Anode for Lithium-Ion Batteries. *Electrochimica Acta*, **404**; 139747

Sirisangsawang, R. and N. Phetyim (2023). Optimization of Tannin Extraction from Coconut Coir through Response Surface Methodology. *Heliyon*, **9**(2); e13377

Sriyanti, I., M. R. Almafie, R. Dani, M. K. N. Ap Idjan, R. U. Partan, M. R. Sanjaya, and J. Jauhari (2023). The Influence of Electrospinning Process Parameters of Polyvinylidene Fluoride and Polyacrylonitrile (PVDF/PAN) Nanofiber Composites. *Jurnal Penelitian Pendidikan IPA*, **9**(9); 7159–7169

Sriyanti, I., L. Marlina, A. Fudholi, S. Marsela, and J. Jauhari (2021). Physicochemical Properties and *In vitro* Evaluation Studies of Polyvinylpyrrolidone/cellulose Acetate Composite Nanofibres Loaded with Chromolaena Odorata (L) King Extract. *Journal of Materials Research and Technology*, **12**; 333–342

Su, Y. P., L. N. Sim, X. Li, H. G. Coster, and T. H. Chong (2021). Anti-Fouling Piezoelectric PVDF Membrane: Effect of Morphology on Dielectric and Piezoelectric Properties. *Journal of Membrane Science*, **620**; 118818

Sui, D., M. Yao, L. Si, K. Yan, J. Shi, J. Wang, C. C. Xu, and Y. Zhang (2023). Biomass-Derived Carbon Coated SiO_2 Nanotubes As Superior Anode for Lithium-Ion Batteries. *Carbon*, **205**; 510–518

Suryani, S., S. Sariani, F. Earnestly, M. Marganof, R. Rahmawati, S. Sevindrajuta, T. M. I. Mahlia, and A. Fudholi (2020). A Comparative Study of Virgin Coconut Oil, Coconut Oil and Palm Oil in Terms of Their Active Ingredients. *Processes*, **8**(4); 402

Triwibowo, J., S. Priyono, I. Purawiardi, T. Lestariningsih, and C. R. Ratri (2016). Study on Electrochemical Performance of Carbon-Coated $LiFePO_4$ As Cathode Material for Lithium Ion Batteries. In *AIP Conference Proceedings*, volume 1755. AIP Publishing, page 150009

Venugopal, N. (2021). Silicon/Spent Coffee Waste-Derived Carbon Composite As an Efficient Anode for Li-Ion Batteries. *International Journal of Electrochemical Science*, **16**(8); 210836

Wang, H., Y. Fu, R. Liu, J. Xiong, and N. Li (2022a). Water-

proof, Breathable and Infrared-Invisible Polyurethane/silica Nanofiber Membranes for Wearable Textiles. *Dalton Transactions*, **51**(36); 13949–13956

Wang, J., C. Li, S. M. Nyambura, J. Xu, H. Li, C. Geng, X. Li, X. Feng, and X. Zhu (2022b). Co-Pyrolysis of Food Waste with Coconut Fiber: Thermogravimetric Analyzes and Hydrogen Yield Optimization. *Energy Sources, Part A: Recovery, Utilization, and Environmental Effects*, **44**(4); 10230–10247

Wang, P., J. Bai, K. Li, H. Ma, W. Li, X. Zhu, Y. Sun, and B. Zhao (2021). $NiCo_2N$ Hollow Sphere with Interconnected Nanosheets Shell: A Potential Anode Material for High Performance Lithium-Ion Batteries. *Chemical Engineering Journal*, **425**; 130607

Wang, P., D. Yan, C. Wang, H. Ding, H. Dong, J. Wang, S. Wu, X. Cui, C. Li, and D. Zhao (2022c). Study of the Formation and Evolution of Solid Electrolyte Interface Via *In-situ* Electrochemical Impedance Spectroscopy. *Applied Surface Science*, **596**; 153572

Wang, X., H. Cheng, G. Ye, J. Fan, F. Yao, Y. Wang, Y. Jiao, W. Zhu, H. Huang, and D. Ye (2022d). Key Factors and Primary Modification Methods of Activated Carbon and Their Application in Adsorption of Carbon-Based Gases: A Review. *Chemosphere*, **287**; 131995

Wu, H., J. Zhu, L. Liu, K. Cao, D. Yang, C. Gong, H. Lei, H. Hang, W. Yao, and J. Xu (2021). Intercalation and delamination of Ti_2SnC with high lithium ion storage capacity. *Nanoscale*, **13**(15); 7355–7361

Xia, A., C. Zhao, W. Yu, Y. Han, J. Yi, and G. Tan (2020). Mo-Doped δ-MnO_2 Anode Material Synthesis and Electrochemical Performance for Lithium-Ion Batteries. *Journal of Applied Electrochemistry*, **50**(7); 733–744

Xiang, Z., Y. Chen, J. Li, X. Xia, Y. He, and H. Liu (2017). Submicro-Sized Porous SiO_2/C and SiO_2/C/Graphene Spheres for Lithium Ion Batteries. *Journal of Solid State Electrochemistry*, **21**(8); 2425–2432

Xu, X., D. Martín Yerga, N. E. Grant, G. West, S. L. Pain, M. Kang, M. Walker, J. D. Murphy, and P. R. Unwin (2023). Interfacial Chemistry Effects in the Electrochemical Performance of Silicon Electrodes under Lithium-Ion Battery Conditions. *Small*, **19**(40); 2303442

Yasmeen, S., M. K. Kabiraz, B. Saha, M. Qadir, M. Gafur, and S. Masum (2016). Chromium (VI) Ions Removal from Tannery Effluent Using Chitosan-Microcrystalline Cellulose Composite As Adsorbent. *International Research Journal of Pure and Applied Chemistry*, **10**(4); 1–14

Zelenka, T., T. Horikawa, and D. Do (2023). Artifacts and Misinterpretations in Gas Physisorption Measurements and Characterization of Porous Solids. *Advances in Colloid and Interface Science*, **311**; 102831

Zhang, T., H. Wei, J. Gao, S. Chen, Y. Jin, C. Deng, S. Wu, H. Xiao, and W. Li (2022a). Synthesis of Sulfonated Hierarchical Carbons and Theirs Application on the Production of Furfural from Wheat Straw. *Molecular Catalysis*, **517**; 112034

Zhang, Y., J. Li, H. Li, H. Shi, Z. Gong, T. Lu, and L. Pan (2022b). Facile Self-Assembly of Carbon-Free Vanadium Sulfide Nanosheet for Stable and High-Rate Lithium-Ion Storage. *Journal of Colloid and Interface Science*, **607**; 145–152

